Hydrogenated core-shell MAX@K2Ti8O17 pseudocapacitance with ultrafast sodium storage and long-term cycling.

ZOU, G., GUO, J., LIU, X., ZHANG, Q., HUANG, G., FERNANDEZ, C. and PENG, Q.

2017

Article type: Full Paper

Hydrogenated Core-Shell MAX@K$_2$Ti$_8$O$_{17}$ Pseudo-capacitance with Ultra-Fast Sodium Storage and Long-Term Cycling

Guodong Zou, Jianxin Guo, Xianyu Liu, Qingrui Zhang, Gang Huang, Carlos Fernandez, and Qiuming Peng*

G. Zou, J. Guo, X. Liu, Prof. Q. Peng

State Key Laboratory of Metastable Materials Science and Technology, Yanshan University,

Qinhuangdao 066004, China

Email: pengqiuming@gmail.com

Prof. Q. Zhang

Hebei Key Laboratory of Applied Chemistry, School of Environmental and Chemical

Engineering, Yanshan University, Qinhuangdao 066004, China

Gang Huang

WPI Advanced Institute for Materials Research, Tohoku University, Sendai 980-8577, Japan.

Prof. C. Fernandez

School of Pharmacy and Life Sciences, Robert Gordon University, Aberdeen, AB107GJ, UK

Abstract

Sodium-ion batteries are considered alternatives to lithium-ion batteries for energy storage devices due to their competitive cost and source abundance. However, the development of electrode materials with long-term stability and high capacity remains a great challenge. Here, we describe for the first time the synthesis of a new class of core-shell MAX@$K_2Ti_8O_{17}$ by alkaline hydrothermal reaction and hydrogenation of MAX, which high sodium ion-intercalation pseudo-capacitance. This composite electrode displays extraordinary reversible capacities of 190 mA h g^{-1} at 200 mA g^{-1} (0.9 C, theoretical value of ~ 219 mA h g^{-1}) and 150 mA h g^{-1} at 1000 mA g^{-1} (4.6 C). More importantly, a reversible capacity of 75 mA h g^{-1} at 10000 mA g^{-1} (46 C) is retained without any apparent capacity decay even after more than 10000 cycles. Experimental tests and first-principle calculations confirm that the increase in Ti^{3+} on the surface layers of MAX@$K_2Ti_8O_{17}$ by hydrogenation increases its conductivity in addition to enhancing the sodium-ion intercalation pseudo-capacitive process. Furthermore, the distorted dodecahedrons between Ti-O layers not only provide abundant sites for sodium-ion accommodation but also act as wide tunnels for sodium-ion transport.

Keywords: hydrogenation treatment, MAX@$K_2Ti_8O_{17}$ composite, electrode, sodium batteries

1. Introduction

Compared with lithium-ion batteries (LIBs), sodium-ion batteries (NIBs) have attracted extraordinary attention because of their low cost, abundant raw materials and environmental friendliness. [1] However, a major challenge to their practical implementation is that they suffer from a lack of suitable electrode materials,[2] to reversibly store a substantial amount of large Na ions (1.02 Å) in a fast and stable manner.[3] Recent important advances in the development of NIBs have mainly focused on the cathode electrode materials. For example, various layered oxides, such as P2-$Na_x[Fe_{0.5}Mn_{0.5}]O_2$,[4] $NaNi_{0.5}Ti_{0.5}O_2$, [5] and P2–Na_xCoO_2,[6] polyanion-based compounds of $Ti_3C_2(OH_xF_{1-x})_2$,[7] $Na_3V_2(PO_4)_3$,[8] $Na_2MnP_2O_7$,[9] and Prussian blue have been tested as promising cathode materials for NIBs.[10] In contrast, there have been limited investigations on anode materials of NIBs. Among the various reported anode materials, carbon materials offer good electrochemical performance[11]. Unfortunately, more than half of their discharge capacity lies in a very low discharge plateau in a range of 0 ~ 0.1 V *vs.* Na^+/Na, resulting in potential safety issues.[3] Organic materials have also been tested, but their electrical conductivity and cyclability need to be further improved. [12] In addition, although high initial capacities are obtained in alloy or sulfide anode materials, large

volume fluctuations and sluggish kinetics decrease their cyclability. [13-14] In addition to the aforementioned anode candidates, the suitable voltages of TiO_2 and its compounds make them promising anode materials for NIBs.[15] However, their cycle capability and conductivity are still not satisfactory for the long-term operation of large-scale energy storage devices, especially at high charge–discharge rates.

More recently, pseudo-capacitive charge storage has been confirmed to significantly improve the rate performance and reversibility of LIBs independent of the limitation from solid-state diffusion.[16] Pioneering work by Dunn and co-workers opens a new paradigm for the design of high-performance electrode materials based on a pseudo-capacitive intercalation mechanism.[16-17] To date, the development of Na-titanates (NTOs) and their related NTO-carbon based composites [18, 21, 22] is considered one of the most successful developments in NIBs.[19, 24-28] However, their limited capacity (low NTO loading), weak interfacial adherence of different composites and unsatisfied cycle stability severely restrict their applications.

Herein, we report a new type of $MAX@K_2Ti_8O_{17}$ composite that was discovered accidently when we used KOH solvent to remove the "A" layer in MAX by a hydrothermal method.[18] The MAX phase reflects the chemical composition of the designated compound family, i.e., $M_{n+1}AX_n$ (n=1,2,3), where M represents an early transition metal, A is assigned to the elements of Group IIIA or IVA and X refers to a C or N component.[19] Interestingly,

WILEY-VCH

taking Ti_3SiC_2 as an example, the Ti_3SiC_2 transforms in situ into nanosheet $K_2Ti_8O_{17}$ on the surface of MAX after alkaline hydrothermal treatment, resulting in the formation of a core-shell composite. These composites have two merits for use as electrode materials. The Ti_3SiC_2 core has superior electrical conductivity ($\sim 10^3$ S /cm), [20] which is much higher than that of activated carbons ($\sim 10^{-1}$ S/cm).[21] Additionally, the $K_2Ti_8O_{17}$ surface layer of $MAX@K_2Ti_8O_{17}$, analogously to NTO, possesses a three-dimensional tunnel framework, which could serve as an excellent host for fast ion transport.[22] As a result, this hydrogenated composite, as an anode of NIBs, delivers high rate capacity and enhanced cycle stability. These values exceed those of almost all other high-performance Ti-based materials reported so far.

2. Results and discussion

2.1. Morphology and structure of core-shell H-KTO

The reaction process is illustrated in **Scheme 1.** The precursor gray Ti_3SiC_2 (TSC, one of typical MAX materials) powders with a dimension of $\sim$ 3 μm were prepared by a heat-pressure sintering method according to the similar processes for Ti_3AlC_2 that we previously reported.[23] After the hydrothermal reaction in KOH solution (the detailed procedure is described in the Methods section) followed by annealing under either pure Ar gas or mixed Ar/H$_2$ gas (hereafter referred to as the hydrogenation treatment), black powders are attained in the former, while it becomes darker in the latter (**Figure S1a-1c**). In contrast to

This article is protected by copyright. All rights reserved.

5

pristine TSC which contains Ti, Si and C, some K and O are detected by energy dispersive

X-ray spectroscopy (EDX) (**Figure S1d-1i**). According to the X-ray diffraction (XRD)

patterns of the products (**Figure 1a)**, the as-sintered samples are mostly indexed to the

Ti_3SiC_2 phase (JCPDF No. 74-0310), wherein some weak TiC peaks (~ 2 wt.%) that formed

during the sintering process are involved.[23] The sample after KOH hydrothermal reaction

followed by the hydrogenation treatment is mainly composed of Ti_3SiC_2 and $K_2Ti_8O_{17}$

(JCPDF No. 41-1100) phases. The concentration of $K_2Ti_8O_{17}$ is ~ 40 wt.% based on both

inductively coupled plasma (ICP) and EDX analysis (**Table S1-S2**). Comparatively, the same

phase compositions are detected after the hydrogenation treatment.

The morphology of the products is observed by field-emission scanning electron

microscopy (FESEM) and transmission electron microscopy (TEM). Both Ar

protection-treated and hydrogenated samples show similar morphologies (**Figure 1b and

Figure S2**). Specifically, urchin-like particles that are covered with fine nanosheets are

distinctly observed. Additionally, the nanosized porous surface is formed by connective

nanosheets (**Figure 1c**), which is supported by the following nitrogen adsorption-desorption

measurement. The higher magnification images (**Figure 1d-f**) reveal that numerous

nanosheets arrays exist on the surface of TSC, forming a core-shell MAX@ $K_2Ti_8O_{17}$

composite. The dimension of the TSC cores is ~ 300 nm. The length and width of the exterior

layer ($K_2Ti_8O_{17}$, marked as KTO) are ~ 150 and ~10 nm, respectively. High resolution TEM

images of the nanosheet in **Figure 1e and Figure S2e** display clear lattice spacings of 0.78

and 0.68 nm, respectively, corresponding to the (200) and (-201) planes of the KTO phase.

Compared with the Ar protection-treated MAX@ $K_2Ti_8O_{17}$ composite (simplified as A-KTO),

a thin amorphous layer of ~ 1.5 nm (**Figure 1e**) is detected on the surface of the

hydrogenated MAX@ $K_2Ti_8O_{17}$ (denoted as H-KTO), which is also evidenced by the weak

amorphous halo in the selected area electron diffraction pattern (SAED, inset in **Figure 1c**)

and the broadened (200) peak (**Figure S2f**).

To understand the formation process of the core-shell structure, the morphology evolution

is monitored at different reaction times and KOH concentrations. As the reaction proceeds,

the surface first becomes coarse, with the formation of irregularly sized particles (**Figure S3**),

indicating that the surface region of TSC was transformed into KTO. With increasing

incubation time, the size of the TSC core decreases, and urchin-like morphology is achieved

(24 h). However, some coarsening KTO bars are observed with further increasing reaction

times. The maximum concentration of the KTO product is ~ 40wt.% (**Figure 1f**).

Additionally, the reaction scarcely occurs when diluting the concentration of KOH.

Comparatively, a higher concentration of KOH leads to coarsened KTO sheets, and the

core-shell structure remains (**Figure S4a-e**).

In addition, the effect of the reaction time on the electrical conductivity (EC) is

investigated (**Figure 1f**). The conductivity is reduced with increasing concentrations of KTO.

Furthermore, the hydrogenation treatment enhanced the EC. The EC of the pristine TSC powder (t=0) is ~ 0.9×10^3 S/cm, slightly lower than the previously reported value of the bulk material.[20] With increasing reaction time, the EC values decrease, down to ~ 1×10^{-3} S/cm when the reaction is over 32 h, remaining there with further increasing incubation time. The effect of KOH on EC values is similar to that of the reaction time (**Figure S4f**). A relatively stable value is attained in 0.5 M for 24 h. Therefore, considering both the amount of KTO and the conductivity, a reaction time of 24 h is desirable, wherein a 40 wt.% $K_2Ti_8O_{17}$ loading and high EC value are achieved.

2.2. Na-ion storage performances

As for the unique morphology and high EC values of A-KTO and H-KTO composites, superior electrochemical performances as anode materials for NIBs are expected. Both composites show similar electrochemical behaviors. The typical cyclic voltammetry (CV) curves of the H-KTO at the initial cycles (**Figure 2a**) show a couple of obvious redox peaks at 0.25/0.69 V, which are assigned to Na-ion insertion/extraction processes.[15a] Comparatively, a weak pair of redox peaks at 1.12/1.25 V might be related to the reversible reaction between Ti^{3+} and Ti^{4+}.[15a] The Coulombic efficiency can be improved from 38 to 88% after a simple presodiation process of contacting with Na metal in the presence of electrolyte for 5 min (**Figure 2b**). Therefore, all the following tests have been performed after a presodiation treatment.

The charge-discharge potential profiles of pure TSC in **Figure S5** reveal that its specific capacity is below 10 mA h g^{-1} and remains stable during subsequent cycling. Thus, the capacity contribution from the core component can be neglected, with the core component appearing to simply act as a conductor for charge collection. The initial discharge capacities of H-KTO and A-KTO after activation are ~210 mA h g^{-1} (**Figure S6**) and ~148 mA h g^{-1} (**Figure S7a**) at 200 mA g^{-1}, respectively. However, the corresponding values decrease to ~195 mA h g^{-1} and ~100 mA h g^{-1} in the fifth cycles. Attractively, the H-KTO electrode delivers a specific capacity of 189 mA h g^{-1} at 200 mA g^{-1} after 200 cycles (**Figure 2c**), 145 mA h g^{-1} at 1000 mA g^{-1} after 1000 cycles and 93 mA h g^{-1} at 6000 mA g^{-1} after 5000 cycles (**Figure S7b-c**). These results demonstrate that the hydrogenation treatment can remarkably improve the capacity (about double) and cyclic stability in contrast to those of A-KTO.[24]

Another attractive property of the H-KTO electrode is its superior rate performance, which is presented in **Figure 2d**. It delivers reversible capacities of 218, 174, 153, 135 and 118 mA h g^{-1} at rates of 200, 500, 1000, 3000 and 6000 mA g^{-1}, respectively. More excitingly, a surprisingly high capacity of more than 80 mA h g^{-1} can be delivered even at an extremely high current density of 10000 mA g^{-1} (46 C). To further confirm the extraordinary rate capability, the H-KTO electrodes are cycled ten times at each current rate (**Figure 2e**). The capacity level remains stable at each rate, regardless of the rapid change in current density. Note that the capacity is gradually restored to ~ 191 mA h g^{-1} at a rate of 200 mA g^{-1},

revealing a remarkable reversibility. Moreover, a reversible capacity of 75 mA h g^{-1} at 10000 mA g^{-1}(46 C) is retained without any notable capacity decay even after more than 10000 cycles (**Figure 3a**).

Importantly, the dimension and core-shell morphology of H-KTO remains unchanged after cycling at such a high rate for 5000 cycles (**Figure 3b**). The phase composition remains the same after 100 cycles (**Figure S8**). These values are higher than those of A-KTO counterparts (**Figure S7d**) and of almost all other high-performance Ti-based materials reported to date (**Figure 2f** [15a, 17c, 24-25]**and Figure 3c**[2b, 15a, 17c, 24, 25b, 25c, 26]). To the best of our knowledge, this is the first time that a combination of extraordinary rate performance and long cycle lifetime with superior capacity retention has been achieved in potassium titanate electrode materials. To confirm the maintained structure during the Na-ion insertion and extraction, *ex situ* XRD measurements were performed. There is no sign of additional peaks associated with other types of structures during the cycling, revealing that there is no evident appearance of a new phase (**Figure S9**). The main peaks display continued shifts as the discharge-charge proceeds.

2.3. Na kinetics analysis

To interpret the superior capacity and rate performance of Na storage behavior, the kinetics of both A-KTO and H-KTO samples have been analyzed by cyclic voltammogram (CV) techniques.[16, 27] In contrast to the A-KTO sample (**Figure S10**), the H-KTO sample (**Figure 4a)** displays similar CV curves with broad peaks during both cathodic and anodic processes

at various sweep rates ranging from 0.10 to 100 mV s^{-1}. According to the relationship

between the measured peak current (i) and the scan rate (v):[27-28]

$$i=av^b \qquad\qquad (1)$$

where a is a constant, b can be determined by the slope of the log(v)–log(i) plots. A b value of

0.50 indicates that the current is controlled by a diffusion process, whereas a value of 1.00

represents a surface-capacitive controlled process. As shown in **Figure 4b**, high b values of

0.96 (cathodic peak) and 0.97 (anodic peak) are observed in the scan rate range of 0.10-5 mV

s^{-1}, and they change to 0.75 and 0.71 in the range of 5–100 mV s^{-1}, respectively, suggesting

that the kinetics of H-KTO exhibits capacitive characteristics. Similar phenomena are also

observed in T-Nb$_2$O$_5$ oxide electrodes.[17a] The rate capability is mainly determined by an

increase in the ohmic contribution and/or diffusion constraint upon a fast scan rate. Based on

the classical Trasatt's method,[29] the plot of capacity *versus* v$^{-1/2}$ demonstrates that the

capacity does not vary significantly as the scan rate increases within the range of 0.10–

1.5 mV s^{-1} (**Figure 4c**). Thus, the total capacitive contribution at a certain scan rate is

calculated by separating the specific capacity contribution from the capacitive and

diffusion-controlled charges at a fixed voltage.[27] As shown in **Figure 4d**, quantitative

calculation results show that the capacitive capacity is gradually improved by increasing the

scan rate, reaching a maximum value of 82.1% at 1.50 mV s^{-1}.

The relationship between kinetics and the electrochemical performance is also measured by electrochemical impedance spectroscopy (EIS). Nyquist plots (**Figure S11a**) of the A-KTO and H-KTO electrodes after activation in frequencies over the range of 100 kHz to 0.10 Hz show the same feature of a depressed semicircle at high frequency, (charge-transfer resistance -R_{ct}) and a linear part at low frequency, (Warburg impedance -Z_w). The smaller R_{ct} for H-KTO (**Table S2**) confirms that the Na reaction kinetics is improved after the hydrogenation treatment. In addition, based on the X-ray photoelectron spectroscopy (XPS) results (**Figure S11b-c**), the shift of the Ti 2p peaks shows that the amount of Ti^{3+} significantly increased after the hydrogenation treatment, which enhances the electrical conductivity.[24] Furthermore, the broadening Ti-O binding (**Figure S11d**) and the decreased O concentration (**Table S3**) reveal the formation of oxygen vacancies, which create more tunnels for Na-ion transport.[17f] Finally, differing from other nanosized materials, the similar nitrogen adsorption-desorption curves of A-KTO (70.2 m^2g^{-1}) and H-KTO (79.8 m^2g^{-1}) (**Figure S12**) demonstrate that the hydrogenation treatment exerts nearly no effect on the core-shell structure. Therefore, the enhanced capacity and kinetics are related to high pseudo-capacitance, low charge-resistance and the formation of a high amount of Ti^{3+}, independent of pore structure.

2.4. Na intercalation mechanism

Long-term cyclability is crucial and challenging for rechargeable NIBs, because of the difficulty in the insertion/extraction of large Na ions. Therefore, to clarify the cause of the high Na capacity and outstanding cyclability of H-KTO, its sodium storage mechanisms need to be explored, as they play a guiding role in the design of new electrode materials for NIBs. The Na intercalation process and storage mechanism are investigated based on first-principle calculations. Our $K_2Ti_8O_{17}$ is described by the C2/m space group, containing 8 K, 32 Ti and 68 O atoms per unit cell. After structural optimization, the calculated XRD result is consistent with the experimental one (**Figure 1a**), wherein the K atoms randomly occupy the four sites of the gap (**Figure 5a**). The gap is described as two types of dodecahedrons (**Figure 5b**), where the cycling Na atoms will occupy those dodecahedrons. The shortest K-O distances in the two pristine dodecahedron lattices are 0.2650 and 0.2881 nm, respectively. The layered structure has a stair-stepping shape, in which it is connected by edge- and corner-sharing TiO_6 octahedrons. The large gaps between TiO_6 octahedrons provide some open channels for Na^+ transport.

The results revealed that the Na atom is prone to being inserted into the middle site (**Figure 5c**) rather than substituting for the K atom, because this insertion has the lowest intercalation energy of 1.20 eV when one Na atom is introduced to KTO (**Figure S13a**). The intercalation energy is 0.30 eV when a K atom is replaced by a Na atom. Similarly, when two Na atoms are intercalated, the most stable structure corresponds to the direct occupation of

empty sites instead of the substitution of K atoms (**Figure S13b**). However, when there are three intercalated Na atoms, they will replace one (-0.29 eV) or two K atoms (-0.26 eV) (**Figure S14**). Finally, the four sites are fully occupied by Na atoms when four Na atoms are intercalated (**Figure 5d and Figure S15**). The shortest Na-O distances in the two fully Na-occupied dodecahedron lattices shift to 0.2491 and 0.2566 nm (**Figure S16a**), respectively.

Remarkably, when further increasing the amount of intercalated Na, the distorted dodecahedrons are shared by two Na atoms. The most stable structure (**Figure 5e**) appears to be a "zig-zag" arrangement of five Na atoms, showing the lowest intercalation energy of -0.10 eV. In addition, there are four different types of distorted dodecahedrons (**Figure S16b**), in which the shortest Na-O bonding is 0.2257 nm. Note that the formation energy of a two Na-atom dodecahedron is higher than that of replacing K atoms. Therefore, it is believed that the substitution of two K atoms predominates before forming two Na atoms in the dodecahedron. Similarly, when six Na atoms are intercalated, two deformed dodecahedrons are formed (**Figure 5f**), and the shortest Na-O bonding is 0.2204 nm (**Figure S16c**). However, if seven or more Na atoms are introduced, positive intercalation energies are attained. The bonding of TiO_6 octahedrons is broken and the main layered structure is destroyed. The volume expansion is over 170% (**Figure S17**). These results demonstrate that the reasonable maximum capacity of reversible Na intercalation is six Na atoms (~ 219 mA h

g^{-1}). Noticeably, this value is lower than that of nominal theoretical capacity reported previously ($\sim$ 308 mA h g^{-1}), wherein all Ti^{4+} are reduced to Ti^{3+} (eight Na atoms). [22]

3. Conclusions

We report for the first time a new method to fabricate a core-shell $MAX@K_2Ti_8O_{17}$ composite by alkaline hydrothermal treatment of a MAX (Ti_3SiC_2) precursor. The electrical conductivity and concentration of $K_2Ti_8O_{17}$ are modified by controlling the KOH concentration and the reaction time. The core-shell $MAX@K_2Ti_8O_{17}$ composite is successfully confirmed as a potential electrode material for Na-ion batteries, with a superior rate capability and excellent long-term cyclability. Attractively, a capacity of $\sim$ 75 mA h g^{-1} is retained without apparent capacity fading, even after more than 10000 cycles at a rigorous high rate of 10000 mA g^{-1}. The formation of the characteristic dodecahedron structure provides many reversible sites for Na-ion storage. The hydrogenating process changes the surface state, resulting in high pseudo-capacitance. Therefore, both high Na capacity and extraordinary cycling performance are achieved concurrently. The outstanding advantages of the methodology, such as its low cost, highly stable structure and simple synthetic route, anticipate enormous potential impacts in the exploitation of new MAX composite electrodes due to the high diversity of MAX compositions (over 60).

4. Experimental Section

Synthesis of Ti₃SiC₂: Ti$_3$SiC$_2$ was synthesized using a method similar to that used for Ti$_3$AlC$_2$ that we reported previously.[23] Specifically, commercial Ti (99.5% purity, 325 mesh, Aladdin Reagent), Si (99.9% purity, 40-200 mesh, Aladdin Reagent) and C (99.5% purity, 2–4 μm, Aladdin Reagent) in a 3:1:2 molar ratio were sealed in a polyurethane container with agate balls and ethanol and milled at 400 rpm for 72 h. The mixtures were cold-pressed at 100 MPa in a stainless-steel die with a diameter of 50 mm, and then the green compacts were hot-pressed in graphite dies at 25 MPa under flowing argon. The samples were heated at a rate of 10 °C min^{-1} until reaching 1600 °C and then were maintained there for 2 h. After being hot-pressed, the surfaces of the samples were ground with SiC to remove the graphite layer, and the bulk was milled at 400 rpm for 6 h and sifted through a 300-mesh sieve to obtain the high-purity Ti$_3$SiC$_2$ powder.

Synthesis of H-KTO and A-KTO: All the reagents obtained from Aladdin (Shanghai, China) were of analytical grade and used without any further purification. Prepared Ti$_3$SiC$_2$ (0.5 g) was added to 25 mL of 0.1–2 M KOH and vigorously stirred for 30 min. The dispersion was sonicated for 30 min to get a homogeneous suspension. Then the suspension was poured into a Teflon-lined stainless steel autoclave with a capacity of 50 mL and maintained at 200 °C for 4–48 h. After hydrothermal reaction, the suspension was centrifuged and rinsed three times using deionized water and ethanol, and then dried at 80 °C for 12 h to obtain Ti$_3$SiC$_2$@K$_2$Ti$_8$O$_{17}$ composites. The Ti$_3$SiC$_2$@K$_2$Ti$_8$O$_{17}$ was placed in a tube furnace

and calcined at 500 °C for 2 h with a heating rate of 5 °C/min in H_2/Ar (5:95 by volume) to synthesize the hydrogenated Ti_3SiC_2@$K_2Ti_8O_{17}$ (H-KTO). In contrast, the Ti_3SiC_2@$K_2Ti_8O_{17}$ (A-KTO) was heat-treated under argon atmosphere with the same parameters as H-KTO.

Material characterization: The phase purity and crystal structure of the samples were recorded on an XRD (Rigaku D/MAX-2005/PC) using Cu Kα radiation (λ=1.5406 Å) with a step scan of 0.02° per step and a scan rate of 2 °/min. The morphologies were characterized by FESEM (Hitachi S4800, Japan) and TEM (JEOL JEM-2010) using an accelerating voltage of 200 kV. To remove the unwanted carbon and oxygen on the conductive carbon adhesive tapes, the powders were cold-pressed into cylinders (10 mm in diameter, 10 mm in height) at 10 MPa in a stainless-steel die. Then, the cylinders were adhered to the conductive carbon adhesive tapes. EDX (Horiba, EMAX) mounted on the Hitachi S-4800 FESEM was used to collect elemental compositions and mapping. According to conservation of mass, the percentages of $K_2Ti_8O_{17}$, TiC and Ti_3SiC_2 in each composite can be calculated by the following equations:

$$x = \frac{367}{39} - a \tag{2}$$

$$y = 7b \tag{3}$$

$$z = 1 - x - y \tag{4}$$

where x, y and z were the percentages of $K_2Ti_8O_{17}$, TiC and Ti_3SiC_2 in the composites, respectively. In addition, *a* and *b* were the percentages of the elements K and Si detected by SEM-EDX, respectively. In addition, 10 mg samples were completely dissolved in 8 mL of HNO_3–HCl (1:3) solution and diluted to 100 mg/L by using deionized water. The diluents were examined by ICP (ICAP 6300 Thermo Scientific) to analyze the elemental contents (Ti, Si, K) of the samples. The percentages of $K_2Ti_8O_{17}$, TiC and Ti_3SiC_2 in each composite can also be calculated by equations (2)–(4).

To measure electrical conductivities, the prepared powders were cold-pressed into cylinders using the same methods as for the EDX measurement. The electrical conductivity was measured with a H7756 four-point probe. The specific surface areas and pore sizes were measured by a Micrometrics ASAP2020 using nitrogen gas adsorption at -196 °C (77 K). The surface elemental analysis of the samples was conducted on the XPS (ThermoFisher K-Alpha) using monochromatic Al Kα (1486.71 eV) X-ray radiation (15 kV and 10 mA).

Electrochemical measurements: Electrochemical performance tests were performed using coin-type 2032 cells with sodium metal foil as the counter and reference electrodes. The working electrodes were made of 85 wt.% active material, 5 wt.% acetylene black and 10 wt.% polyvinylidene fluoride (PVDF) in methyl-2-pyrrolidone (NMP). After mixing thoroughly, the slurries were cast on battery-grade copper foil and dried in a vacuum oven at 120 °C for 12 h. The loading amount of active material on each electrode was 1.0–1.5

mg/cm^{-2}, and electrodes were punched as 12 mm discs. All the electrodes were assembled in an argon-filled glove box with moisture and oxygen concentrations below 1 ppm. A glass fiber (GF/D, Whatman) and 1.0 M NaClO$_4$ in a mixture of ethylene carbonate (EC)/ diethyl carbonate (DEC) (1:1 by volume) with 5 vol.% fluorinated ethylene carbonate (FEC) were used as the separator and electrolyte, respectively. A battery measurement system (Land CT2001A) was applied to test galvanostatic charge-discharge cycles at different rates with a voltage window of 0.01–2.5 V. The CV was performed on an electrochemical workstation (Bio-logic, VSP) with a scan rate of 0.1–100 mV/s between 0.01 and 2.5 V. EIS was measured by an electrochemical workstation (Bio-logic, VSP) in the frequency range from 100 kHz to 0.1 Hz with an alternating voltage amplitude of 5 mV.

Computational method and model: The calculations were performed by Viennaab initio Simulation Package (VASP) code with density functional theory (DFT).[30] The exchange-correlation function of the generalized gradient approximation (GGA) with the Perdue-Burke-Ernzerhof (PBE) was performed. The ion-electron interaction was described by the projector augmented wave (PAW) method.[31] A plane wave cutoff energy of 500 eV was used to guarantee the convergency. A 3×12×4 Monkhorst-Pack *k*-point grid was taken during optimization.[32] The structural optimization including the position of atoms was calculated using a conjugated gradient method, and the total energy of the optimized structures was well-converged, with 10^{-6} eV per cell in energy and 0.005 eV/Å in force.

Provided that the whole structure of the pristine matrix can be retained during the charge-discharge process, the cycling stability would be desirable. Therefore, to investigate the maximum capacity of Na intercalation, the following insertion reaction was considered:

$$K_2Ti_8O_{17} + xNa \rightarrow Na_xK_{2-y}Ti_8O_{17} \qquad (5)$$
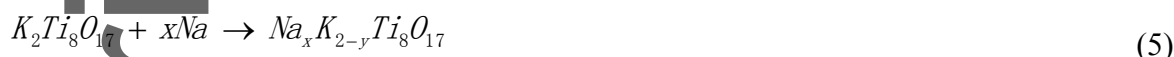
where x was the number of intercalated Na ions, and y was the number of K that was replaced. Thus, the intercalation energies (E_f) per Na atom intercalating into KTO with or without substituting K atoms were defined as the following:

$$E_i = \frac{1}{x}E_{Na_xK_{2-y}Ti_8O_{17}} + xE_{Na} - yE_K$$

(6)

where $E_{Na_xK_{2-y}Ti_8O_{17}}$ was the total energy of $Na_xK_{2-y}Ti_8O_{17}$ with Na atoms and E_{Na}/E_K was the energy per Na/K atom in the Na/K bulk. x and y were the numbers of Na and K, respectively. According to this definition, a negative E_i demonstrates that the Na atoms can intercalate into KTO to form stable structures during cycling.

Supporting Information

Supporting Information is available from the Wiley Online Library or from the author.

Acknowledgments

We greatly acknowledge the NSFC (No. 51422105), the NSF of Hebei (No. E2015203404), the Hebei province scientific program (No. GCC2014058) and the High-Performance Computing Platform of Hebei University. We are grateful to Prof. Hai-Jun Wang at Hebei University for computational support with a "Molecule Aggregated Structure" work-station. We thank Dr. Jianyu Huang for language assistance.

References

[1] B. Dunn, H. Kamath, J.-M. Tarascon, *Science* **2011**, *334*, 928-935.

[2] [a]P. Simon, Y. Gogotsi, B. Dunn, *Science* **2014**, *343*, 1210-1211; [b]C. Wu, Y. Jiang, P. Kopold, P. A. van Aken, J. Maier, Y. Yu, *Adv. Mater.* **2016**, *28*, 7276-7283.

[3] K. Kubota, S. Komaba, *J. Electrochem.Soc.* **2015**, *162*, A2538-A2550.

[4] N. Yabuuchi, M. Kajiyama, J. Iwatate, H. Nishikawa, S. Hitomi, R. Okuyama, R. Usui, Y. Yamada, S. Komaba, *Nat. Mater.* **2012**, *11*, 512-517.

[5] H. Wang, Y. Xiao, C. Sun, C. Lai, X. Ai, *RSC Adv.* **2015**, *5*, 106519-106522.

[6] R. Berthelot, D. Carlier, C. Delmas, *Nat. Mater.* **2011**, *10*, 74-80.

[7]   X. Xie, M.-Q. Zhao, B. Anasori, K. Maleski, C. E. Ren, J. Li, B. W. Byles, E. Pomerantseva, G. Wang, Y. Gogotsi, *Nano Energy* **2016**, *26*, 513-523.

[8]   Z. Jian, L. Zhao, H. Pan, Y.-S. Hu, H. Li, W. Chen, L. Chen, *Electrochem. Commun.* **2012**, *14*, 86-89.

[9]   C. S. Park, H. Kim, R. A. Shakoor, E. Yang, S. Y. Lim, R. Kahraman, Y. Jung, J. W. Choi, *J. Am. Chem. Soc.* **2013**, *135*, 2787-2792.

[10] X. Xie, M. Ye, C. Liu, P.-C. Hsu, C. S. Criddle, Y. Cui, *Energy Environ. Sci.* **2015**, *8*, 546-551.

[11] H. Hou, X. Qiu, W. Wei, Y. Zhang, X. Ji, *Adv. Energy Mater.* **2017**, *doi: 10.1002/aenm.201602898*.

[12] B. V. Ratnakumar, S. Di Stefano, R. M. Williams, G. Nagasubramanian, C. P. Bankston, *J. Appl. Electrochem.* **1990**, *20*, 357-364.

[13] I. S. Kim, P. N. Kumta, G. E. Blomgren, *Electrochem. Solid-State Lett.* **2000**, *3*, 493-496.

[14] W. Sun, X. Rui, D. Zhang, Y. Jiang, Z. Sun, H. Liu, S. Dou, *J. Power Sources* **2016**, *309*, 135-140.

[15] [a]Y. Zhang, C. W. Foster, C. E. Banks, L. Shao, H. Hou, G. Zou, J. Chen, Z. Huang, X. Ji, *Adv. Mater.* **2016**, *28*, 9391-9399; [b]T. Brezesinski, J. Wang, J. Polleux, B. Dunn, S. H.

Tolbert, *J. Am. Chem. Soc.* **2009**, *131*, 1802-1809; [c]D. Su, S. Dou, G. Wang, *Chem. Mater.* **2015**, *27*, 6022-6029.

[16] V. Augustyn, J. Come, M. A. Lowe, J. W. Kim, P.-L. Taberna, S. H. Tolbert, H. D. Abruña, P. Simon, B. Dunn, *Nat. Mater.* **2013**, *12*, 518-522.

[17] [a]J. W. Kim, V. Augustyn, B. Dunn, *Adv. Energy Mater.* **2012**, *2*, 141-148; [b]S. Dong, L. Shen, H. Li, G. Pang, H. Dou, X. Zhang, *Adv. Func.Mater.* **2016**, *26*, 3703-3710; [c]H. Yu, Y. Ren, D. Xiao, S. Guo, Y. Zhu, Y. Qian, L. Gu, H. Zhou, *Angew. Chem. Int. Edit.* **2014**, *126*, 9109-9115; [d]V. Augustyn, P. Simon, B. Dunn, *Energy Environ. Sci.* **2014**, *7*, 1597-1614; [e]S. Li, J. Qiu, C. Lai, M. Ling, H. Zhao, S. Zhang, *Nano Energy* **2015**, *12*, 224-230; [f]H.-S. Kim, J. B. Cook, H. Lin, J. S. Ko, S. H. Tolbert, V. Ozolins, B. Dunn, *Nat. Mater.* **2017**, 16, 454-460.

[18] [a]M. R. Lukatskaya, O. Mashtalir, C. E. Ren, Y. Dall'Agnese, P. Rozier, P. L. Taberna, M. Naguib, P. Simon, M. W. Barsoum, Y. Gogotsi, *Science* **2013**, *341*, 1502-1505; [b]M. Ghidiu, M. R. Lukatskaya, M.-Q. Zhao, Y. Gogotsi, M. W. Barsoum, *Nature* **2014**, *516*, 78-81.

[19] M. Naguib, J. Come, B. Dyatkin, V. Presser, P.-L. Taberna, P. Simon, M. W. Barsoum, Y. Gogotsi, *Electrochem. Commun.* **2012**, *16*, 61-64.

[20] M. W. Barsoum, T. El-Raghy, *J. Am.Ceram. Soc.* **1996**, *79*, 1953-1956.

[21] W. Xu, J. J. Pignatello, W. A. Mitch, *Environ. Sci. Tech.* **2013**, *47*, 7129-7136.

[22] J. Han, M. Xu, Y. Niu, G.-N. Li, M. Wang, Y. Zhang, M. Jia, C. m. Li, *Chem. Commun.* **2016**, *52*, 11274-11276.

[23] Q. Peng, J. Guo, Q. Zhang, J. Xiang, B. Liu, A. Zhou, R. Liu, Y. Tian, *J. Am. Chem. Soc.* **2014**, *136*, 4113-4116.

[24] S. Fu, J. Ni, Y. Xu, Q. Zhang, L. Li, *Nano Lett.* **2016**, *16*, 4544-4551.

[25] [a] J. Ni, S. Fu, C. Wu, Y. Zhao, J. Maier, Y. Yu, L. Li, *Adv. Energy Mater.* **2016**, *6*, 1502568; [b] A. Rudola, K. Saravanan, S. Devaraj, H. Gong, P. Balaya, *Chem. Commun.* **2013**, *49*, 7451-7453; [c] X. Wang, Y. Li, Y. Gao, Z. Wang, L. Chen, *Nano Energy* **2015**, *13*, 687-692.

[26] [a] Y. Wang, X. Yu, S. Xu, J. Bai, R. Xiao, Y.-S. Hu, H. Li, X.-Q. Yang, L. Chen, X. Huang, *Nat. Commun.* **2013**, *4*, 2365; [b] S. Guo, J. Yi, Y. Sun, H. Zhou, *Energy Environ. Sci.* **2016**, *9*, 2978-3006.

[27] C. Chen, Y. Wen, X. Hu, X. Ji, M. Yan, L. Mai, P. Hu, B. Shan, Y. Huang, *Nat. Commun.* **2015**, *6*, 6929.

[28] [a]C. Wu, P. Kopold, Y.-L. Ding, P. A. van Aken, J. Maier, Y. Yu, *ACS Nano* **2015**, *9*, 6610-6618; [b]J. Ni, S. Fu, C. Wu, J. Maier, Y. Yu, L. Li, *Adv. Mater.* **2016**, *28*, 2259-2265.

[29] S. Trasatti, O. A. Petrii, *Pure Appl. Chem.* **1991**, *63*, 711-734.

[30] G. Kresse, J. Furthmüller, *Phys. Rev. B* **1996**, *54*, 11169-11186.

[31] P. E. Blöchl, *Phys. Rev. B* **1994**, *50*, 17953-17979.

[32] H. J. Monkhorst, J. D. Pack, *Phys. Rev. B* **1976**, *13*, 5188-5192.
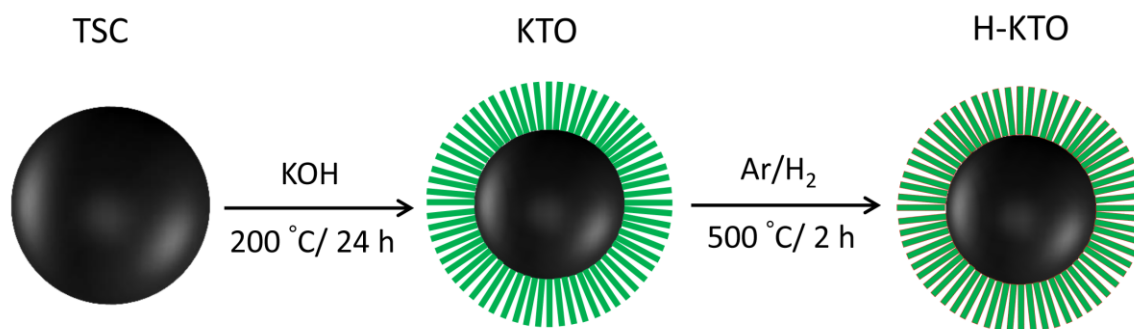
Scheme 1. Reaction process and experimental parameters of H-KTO formation.
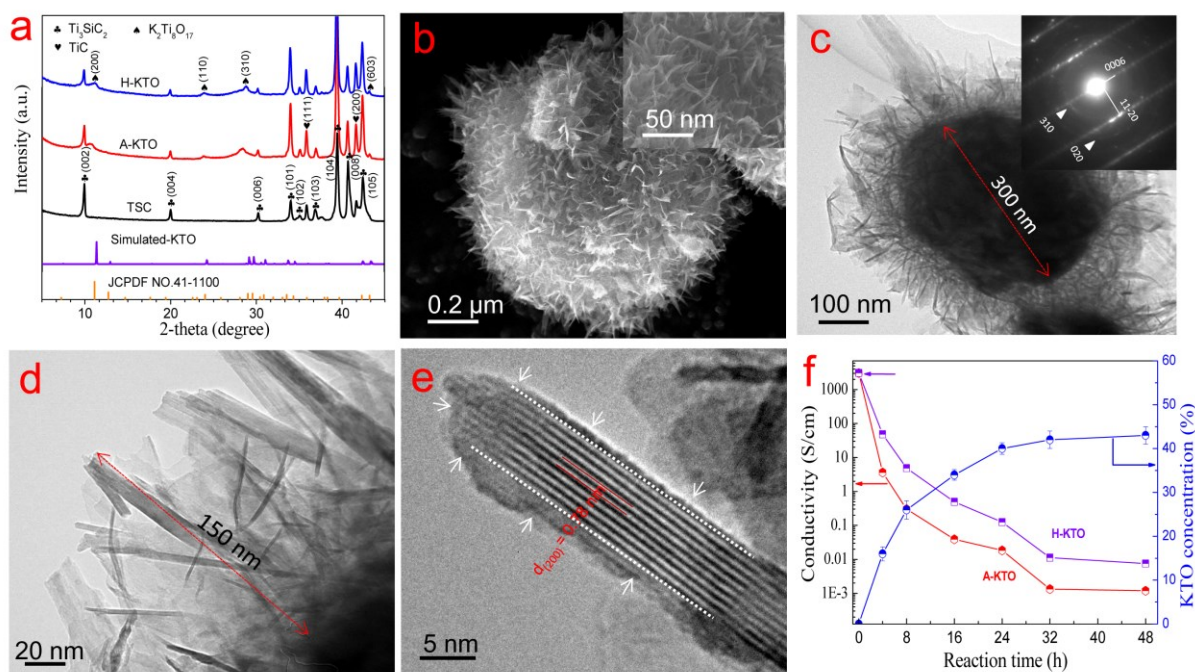
Figure 1. Material characterizations. a) XRD patterns of different samples. b) A representative FESEM image of the H-KTO composite. The inset shows a high magnification of image. c) Typical TEM image of a core-shell H-KTO sample. The inset corresponds to the SAED image of the exterior shell layer ($K_2Ti_8O_{17}$). d) A high magnification of the exterior shell layer ($K_2Ti_8O_{17}$). e) HRTEM image of the $K_2Ti_8O_{17}$ plate. f) Effect of reaction time on the conductivity and KTO concentration of different samples.
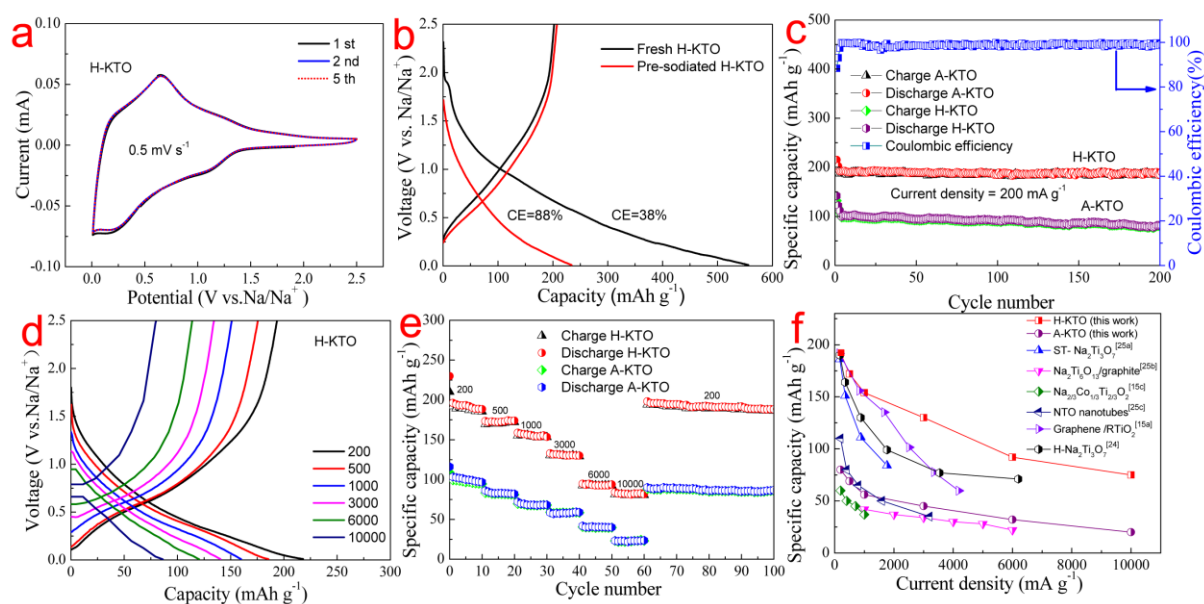
Figure 2. Electrode properties. a) Cyclic voltammograms recorded at a scan rate of 0.5 mV s^{-1} over a voltage range of 0.01–2.5 V versus Na/Na$^+$. b) Initial galvanostatic curves of fresh and pre-sodiated H-KTO electrodes. c) Long-term cycling performance of H-KTO and A-KTO samples at 200 mA g^{-1}. Coulombic efficiency is plotted for the H-KTO sample only. d) First charge-discharge profiles of H-KTO at different current rates. e) Rate performances of H-KTO and A-KTO at different current rates from 200 mA g^{-1} to 10000 mA g^{-1}. f) Comparison of the rate capacities of H-KTO with other reported high-performance Ti-based electrodes at different current densities.
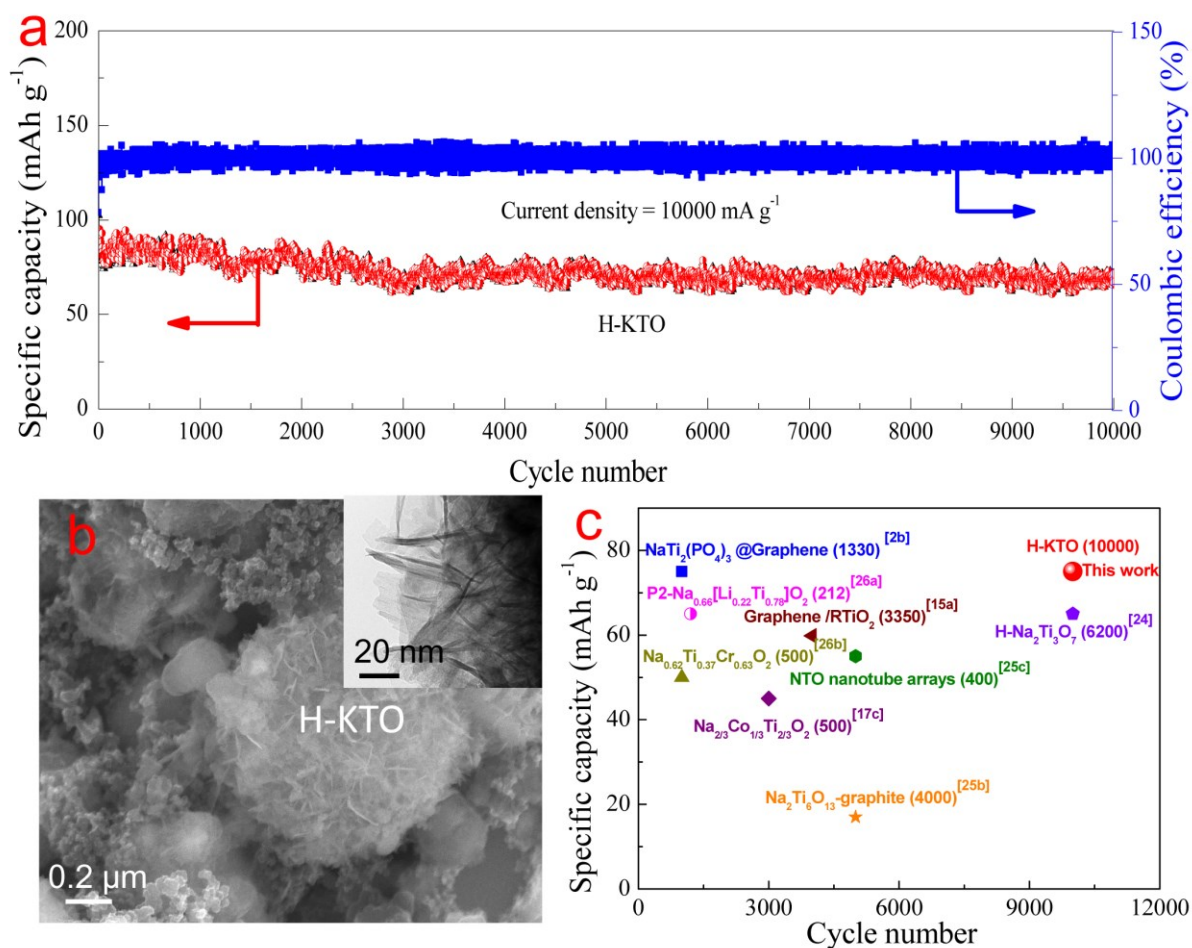
Figure 3. Cycling stability. a) Cycling properties of the H-KTO electrode at a current rate of 10000 mA g^{-1}. b) SEM image of the H-KTO electrode after 5000 cycles at a current density of 10000 mA g^{-1}. The inset corresponds to local high magnification of the shell layer. c) Comparison of specific capacities of Ti-based electrodes at high current rates. The current rate density is shown in parentheses.
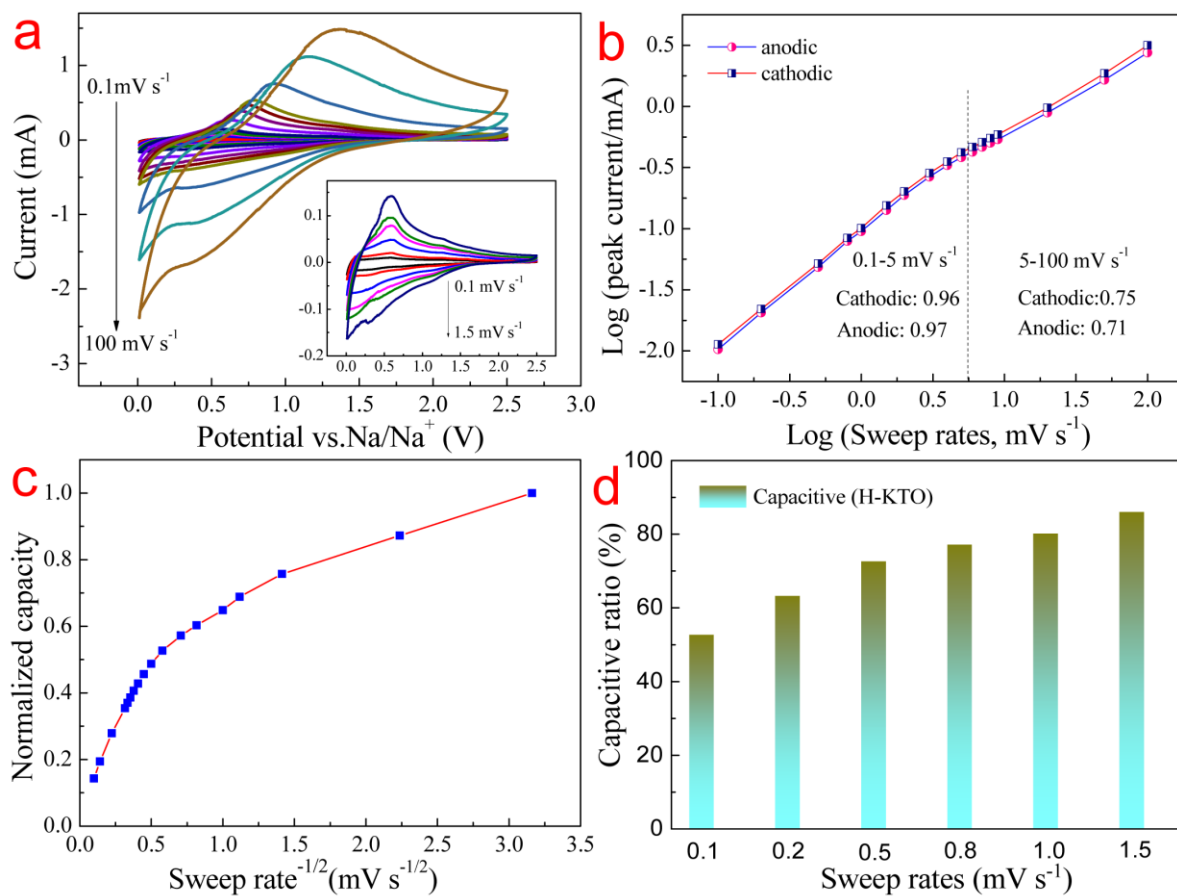
Figure 4. Kinetic analysis of the electrochemical behavior of the H-KTO electrode. a) Cyclic

voltammetry curves at sweep rates from 0.1 to 100 mV s^{-1}. b) b-value determination using

the relationship between the peak currents and the sweep rates. c) The normalized capacity

versus sweep rate$^{-1/2}$. d) Capacitive ratios of the H-KTO electrode at different sweep rates.
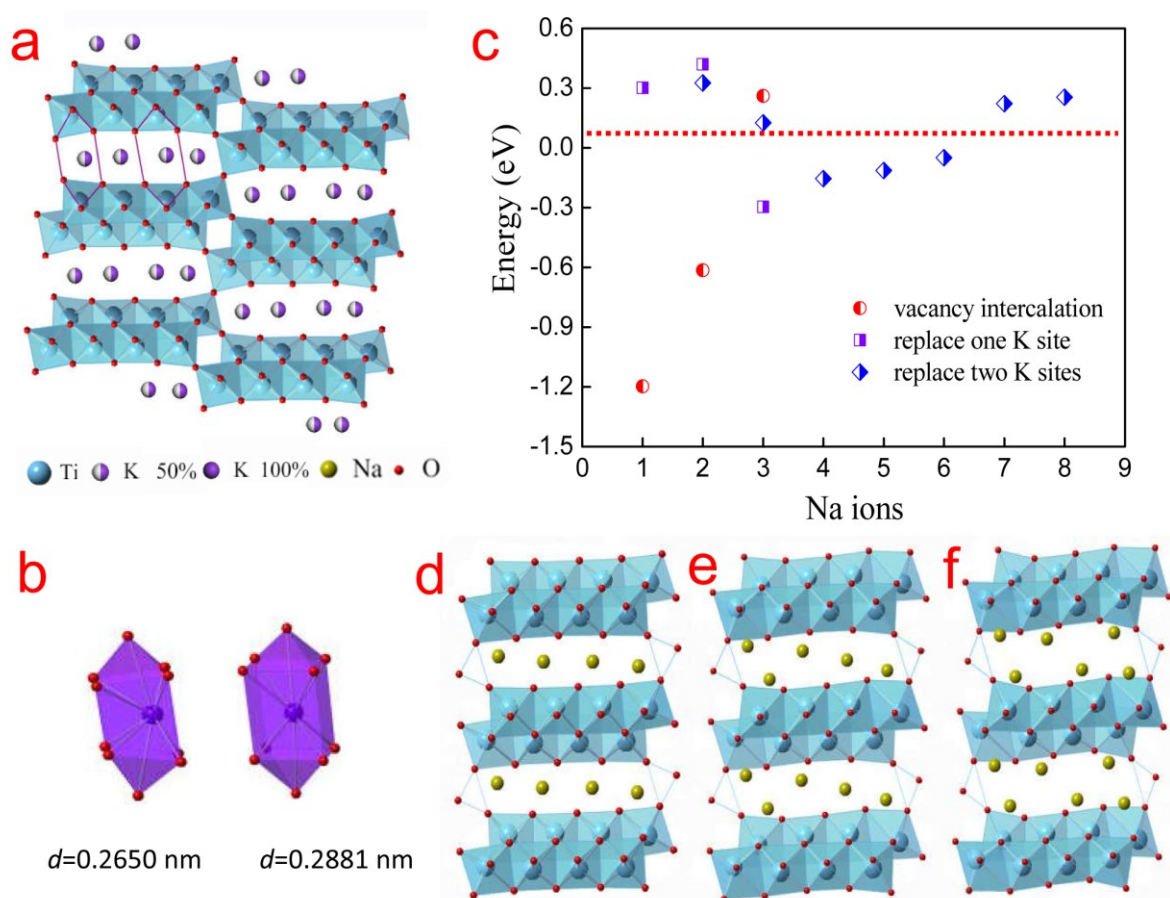
Figure 5. Na intercalation mechanism. a) Typical crystal structure of a KTO sample, wherein the middle layer (4 sites) is equally occupied by two K atoms. b) Two irregular dodecahedrons in the KTO sample for Na occupation, which store one or two sodium atoms. The d_{K-O} values are 0.2650 nm and 0.2881 nm, respectively. c) Energy variation of the KTO sample after intercalating different numbers of Na ions during charge-discharge cycles. Typical stable crystal structure of a KTO sample after Na intercalation, d) 4 Na atoms ($Na_4Ti_8O_{17}$), e) 5 Na atoms ($Na_5Ti_8O_{17}$) and f) 6 Na atoms ($Na_6Ti_8O_{17}$).

The table of contents

We describe a new method to prepare core-shell MAX@$K_2Ti_8O_{17}$ composites by alkalization hydrothermal reaction and hydrogenation, which bestows high sodium-ion intercalation pseudo-capacitance. High capacity and structural stability, especially at high rates, are achieved simultaneously. The method is highlighted by its simplicity and high-yield production of a well-defined morphology, which has promising industrial merits. In addition, this route can be extended to prepare other MAX based electrode materials.

Keywords: Batteries; Pseudo-capacitance

Guodong Zou, Jianxin Guo, Xianyu Liu, Qingrui Zhang, Gang Huang, Carlos Fernandez, and Qiuming Peng*

**ADVANCED
ENERGY
MATERIALS**

Supporting Information

Hydrogenated Core–Shell MAX@$K_2Ti_8O_{17}$ Pseudocapacitance with Ultrafast Sodium Storage and Long-Term Cycling

Guodong Zou, Jianxin Guo, Xianyu Liu, Qingrui Zhang, Gang Huang, Carlos Fernandez, and Qiuming Peng*

WILEY-VCH

Supporting Information

Hydrogenated Core-Shell MAX@K$_2$Ti$_8$O$_{17}$ Pseudo-capacitance with Ultra-Fast Sodium Storage and Long-Term Cycling

Guodong Zou, Jianxin Guo, Xianyu Liu, Qingrui Zhang, Gang Huang, Carlos Fernandez, and Qiuming Peng*

G. Zou, J. Guo, X. Liu, Prof. Q. Peng

State Key Laboratory of Metastable Materials Science and Technology, Yanshan University,

Qinhuangdao 066004, China

Email: pengqiuming@gmail.com

Prof. Q. Zhang

Hebei Key Laboratory of Applied Chemistry, School of Environmental and Chemical

Engineering, Yanshan University, Qinhuangdao 066004, China

Gang Huang

WPI Advanced Institute for Materials Research, Tohoku University, Sendai 980-8577, Japan.

Prof. C. Fernandez

School of Pharmacy and Life Sciences, Robert Gordon University, Aberdeen, AB107GJ, UK

Table S1 Chemical compositions of three samples based on ICP Analysis.

Samples	Elemental composition (mg/L)			$K_2Ti_8O_{17}$ concentration (wt.%)
	Ti	Si	K	
TSC	73.52	14.08	-	-
A-KTO	65.08	8.02	4.26	40.51
H-KTO	65.12	8.32	4.24	40.08

Table S2. The fitting date based on the EIS curves.

Samples	Rs (ohm)	Error (%)	Rct (ohm)	Error (%)	Z_W	Error (%)
A-KTO	5.952	2.248	686.2	1.621	0.105	1.764
H-KTO	4.751	1.089	154.7	0.5128	0.0098	0.8721

Table S3 Chemical compositions of three samples in terms of EDX analysis.

Samples	Elemental percentage (wt.%)					$K_2Ti_8O_{17}$ concentration (wt. %)
	Ti	Si	K	C	O	
TSC	73.59	14.06	-	12.45	-	-
A-KTO	65.18	8.31	4.26	7.44	14.81	40.59
H-KTO	65.78	8.43	4.25	7.62	13.92	39.99
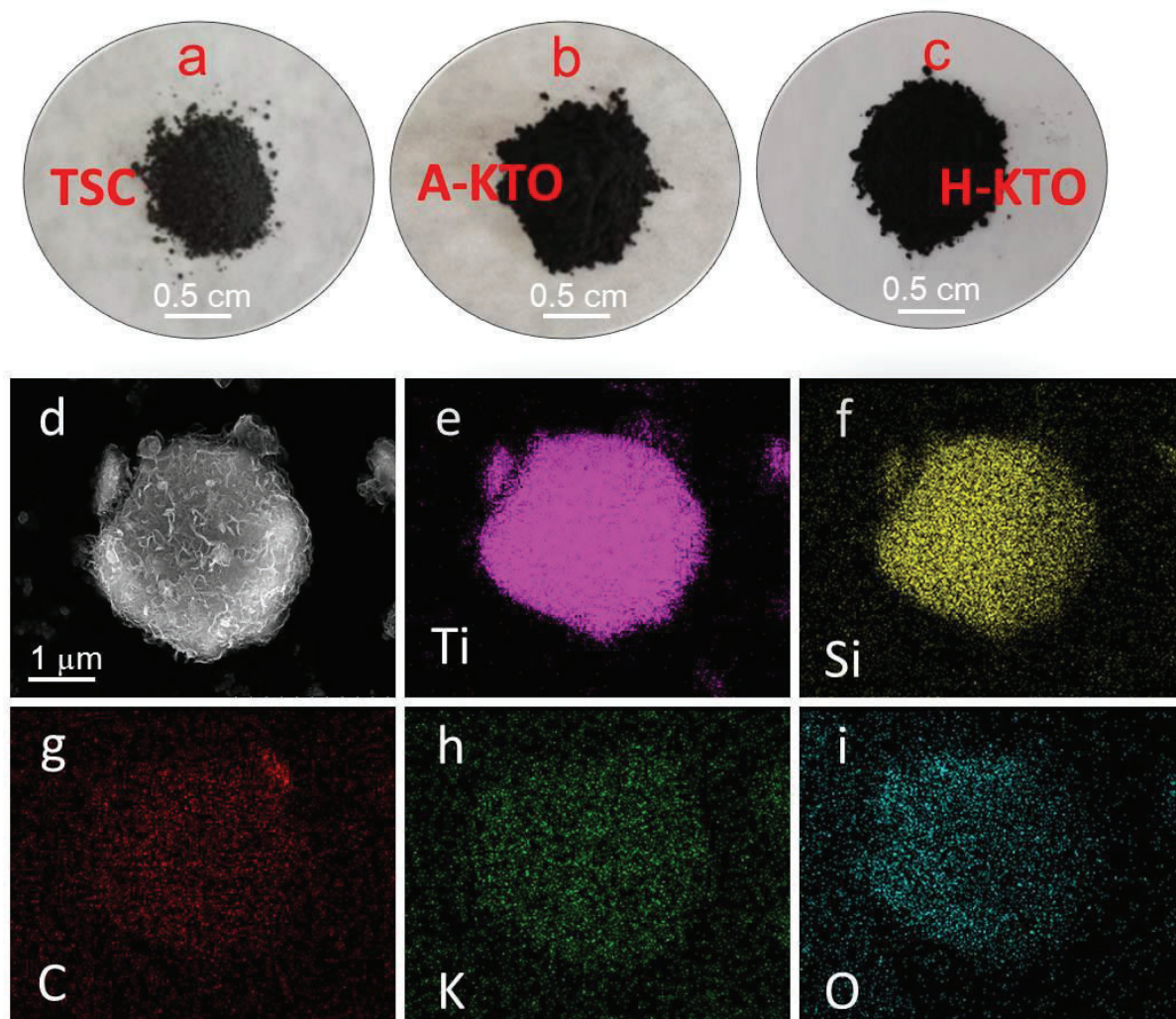
Figure S1. a)-c) Macro-optical graphs of TSC, A-KTO and H-KTO, respectively. d) The typical SEM image of H-KTO sample (0.5 M KOH, 24 h), e)-i) the elemental maps of Ti, Si, C, K and O, respectively.
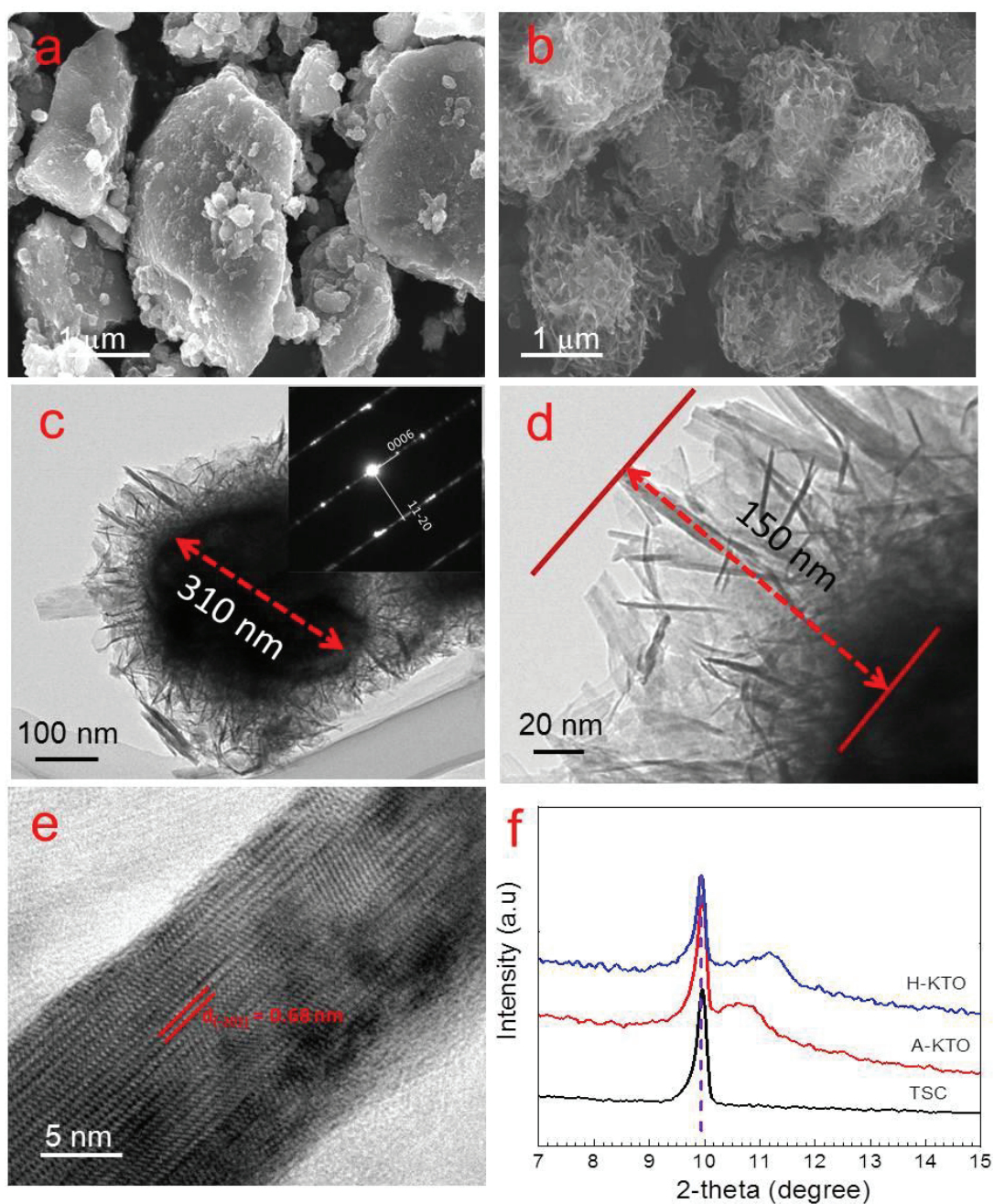
Figure S2. a) Typical FESEM image of Ti$_3$SiC$_2$ particles. b) A representative FESEM image of A-KTO sample. c) TEM image of a core-shell A-KTO sample, the inset corresponds to SAED image of the exterior shell layer (K$_2$Ti$_8$O$_{17}$). d) A high magnification of the exterior shell layer (K$_2$Ti$_8$O$_{17}$). e) HRTEM image of the K$_2$Ti$_8$O$_{17}$ plate in A-KTO sample. f) XRD patterns of different samples in the angle range of 7 ~ 15 degree.
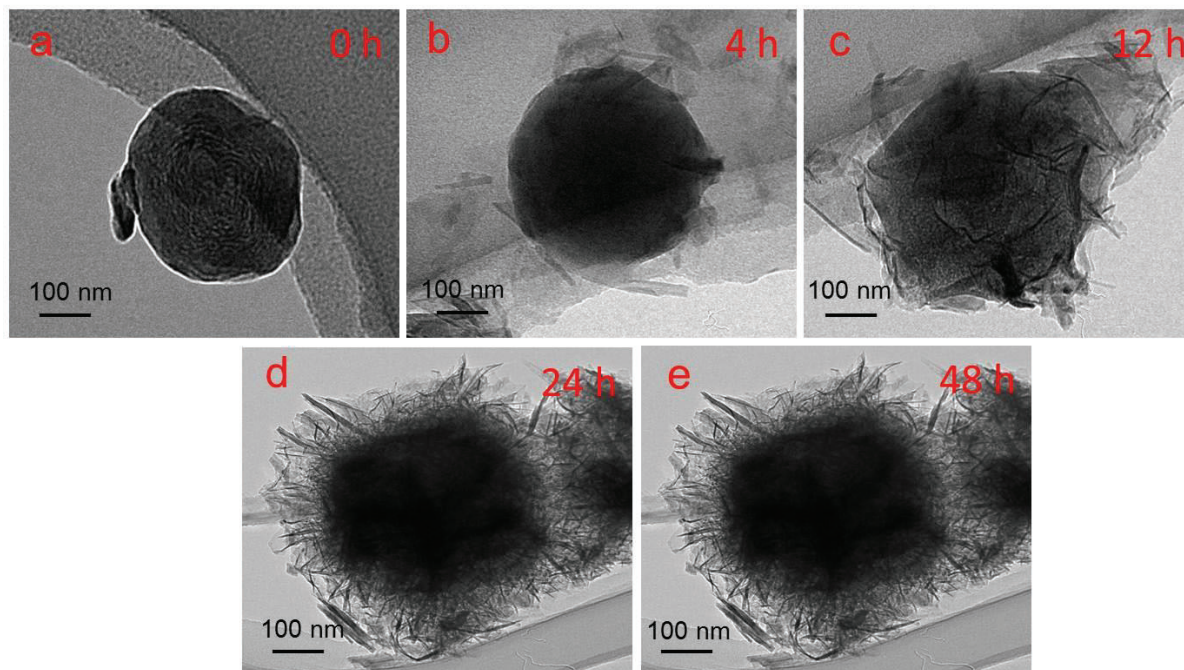
Figure S3. TEM images of the samples containing 0.5 M KOH after different incubation times.
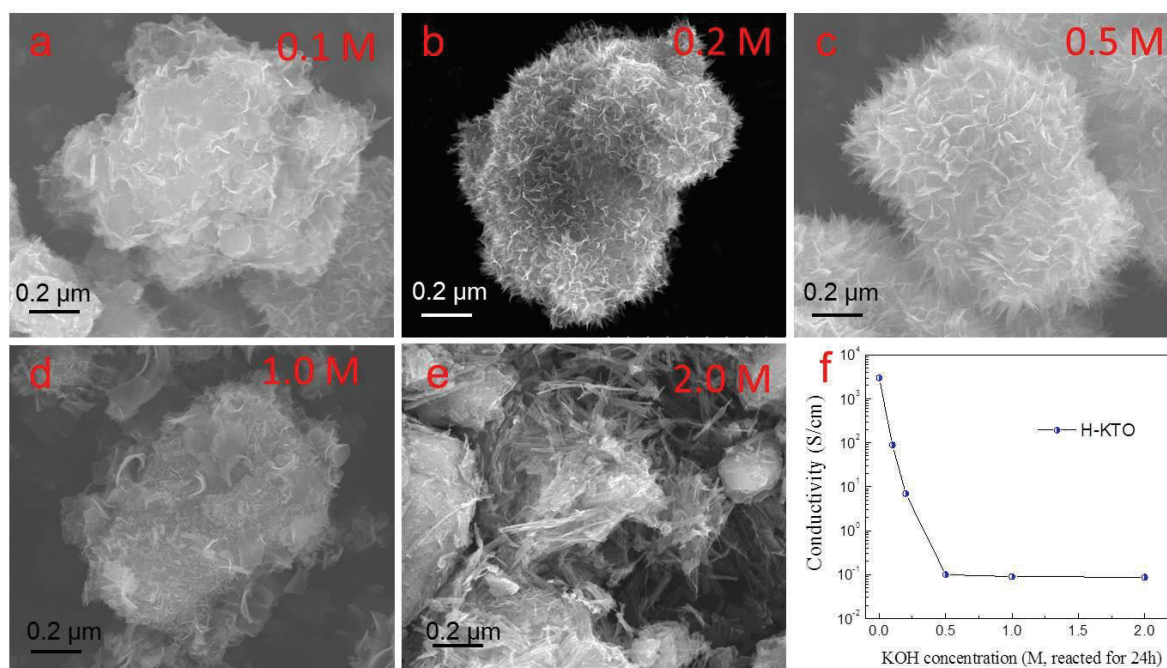
Figure S4. a-e) Morphology variation of the samples dependent on different KOH concentrations. f) The conductivity of H-KTO in different KOH concentrations after reacting for 24 h.
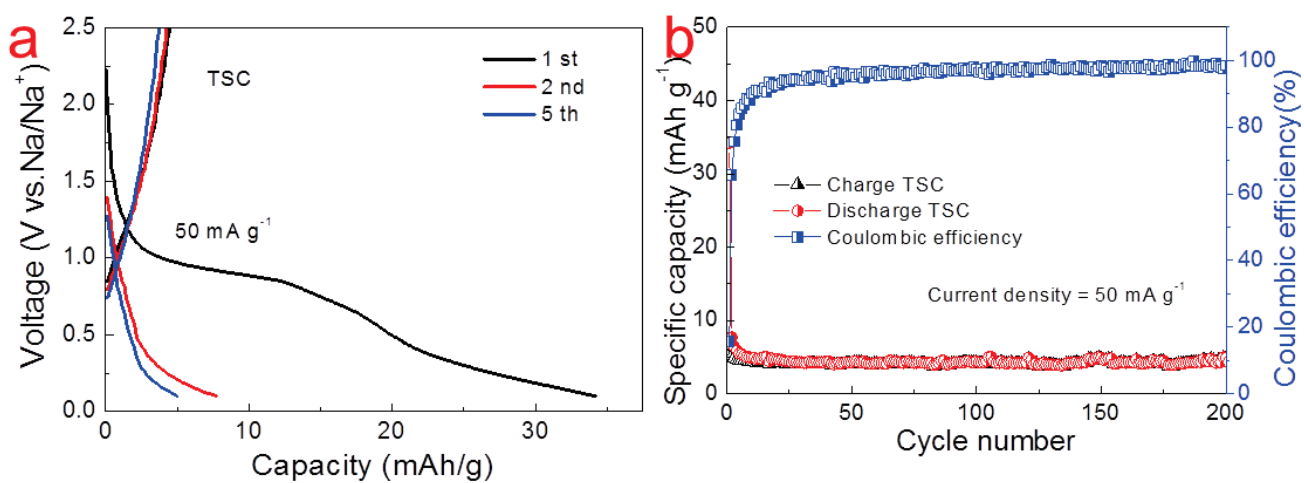
Figure S5. Electrochemical performance of TSC for sodium storage. a) The charge-discharge curves of the TSC at a rate of 50 mA g^{-1} during initial cycles; b) cycling performance of TSC.
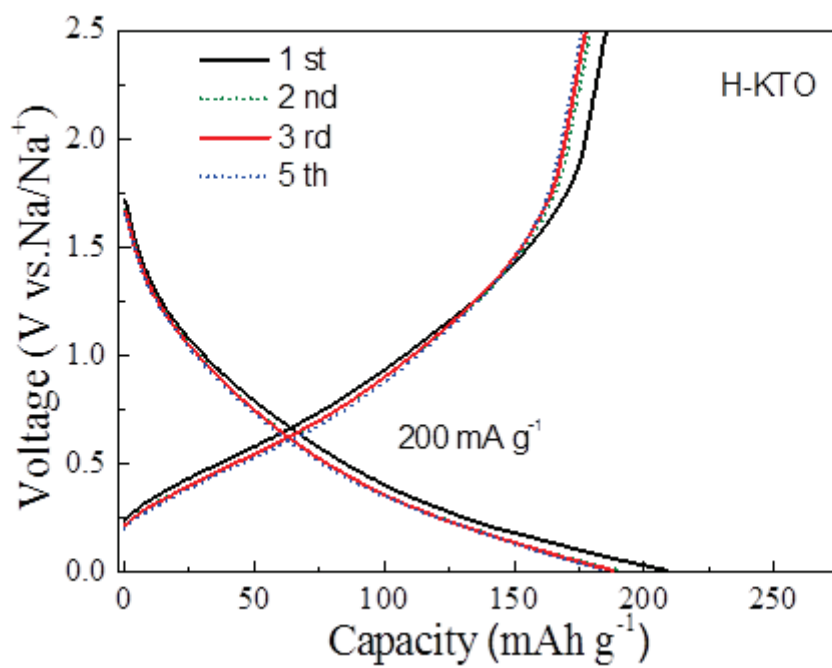
Figure S6 Charge-discharge profiles of H-KTO at the initial cycles at 200 mA g^{-1}.
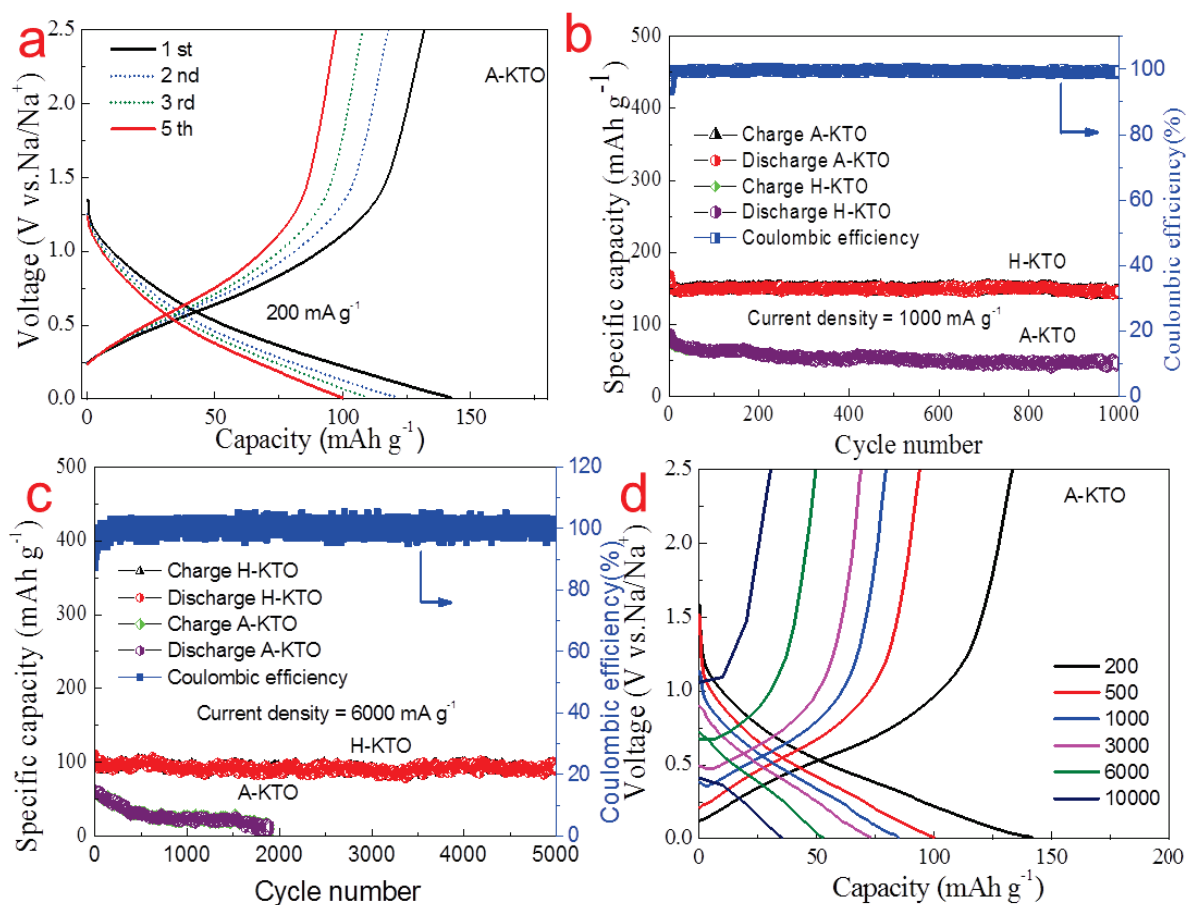
Figure S7. a) Charge-discharge profiles of A-KTO at the initial cycles at 200 mA g^{-1}. b) and c)

Cycling performance of H-KTO and A-KTO samples at1000 mA g^{-1}and 6000 mA g^{-1},

respectively. Coulombic efficiency is plotted for H-KTO sample only. d) First

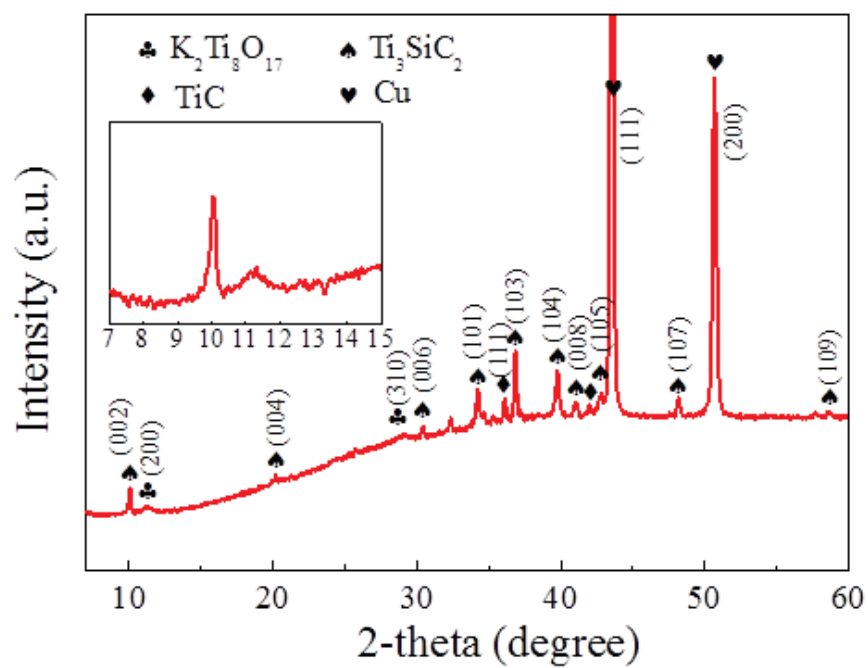charge-discharge profiles of A-KTO at different current rates.

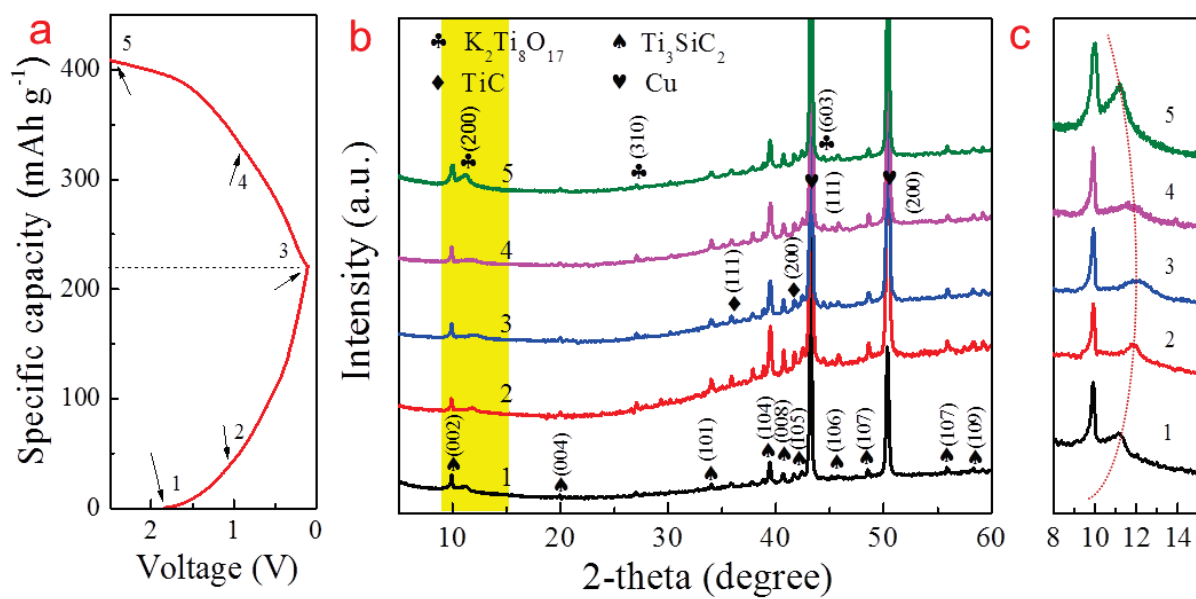**Figure S8.** The XRD pattern of H-KTO after 100 cycles.

Figure S9. *Ex situ* XRD pattern of H-KTO at different states for the fifth cycle. a) A typical charge-discharge curve; b) XRD patterns at different stages; c) high magnification patterns in red area.
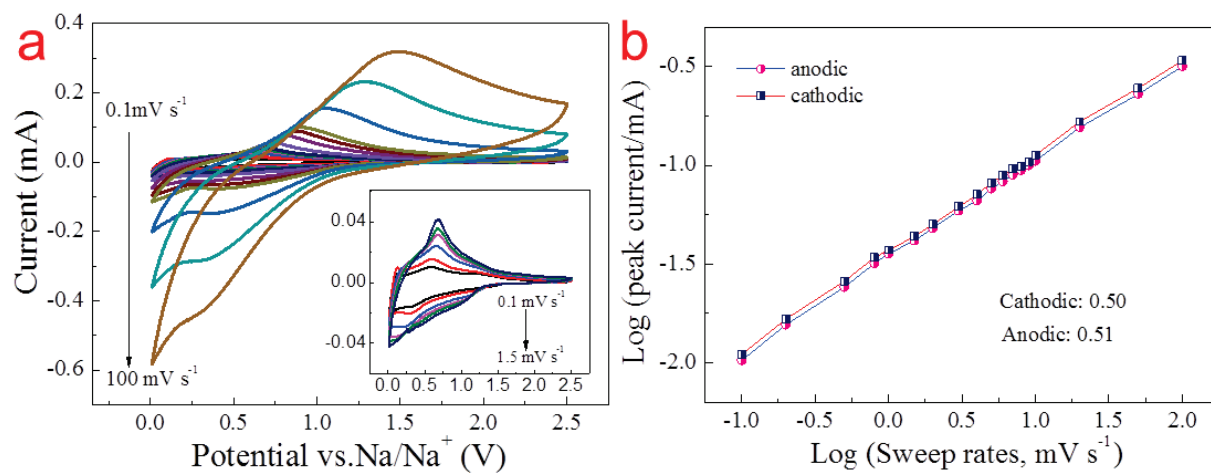
Figure S10. a) Cycle voltammetry curves at sweep rates from 0.1 to 100 mV s^{-1}. b) b-value

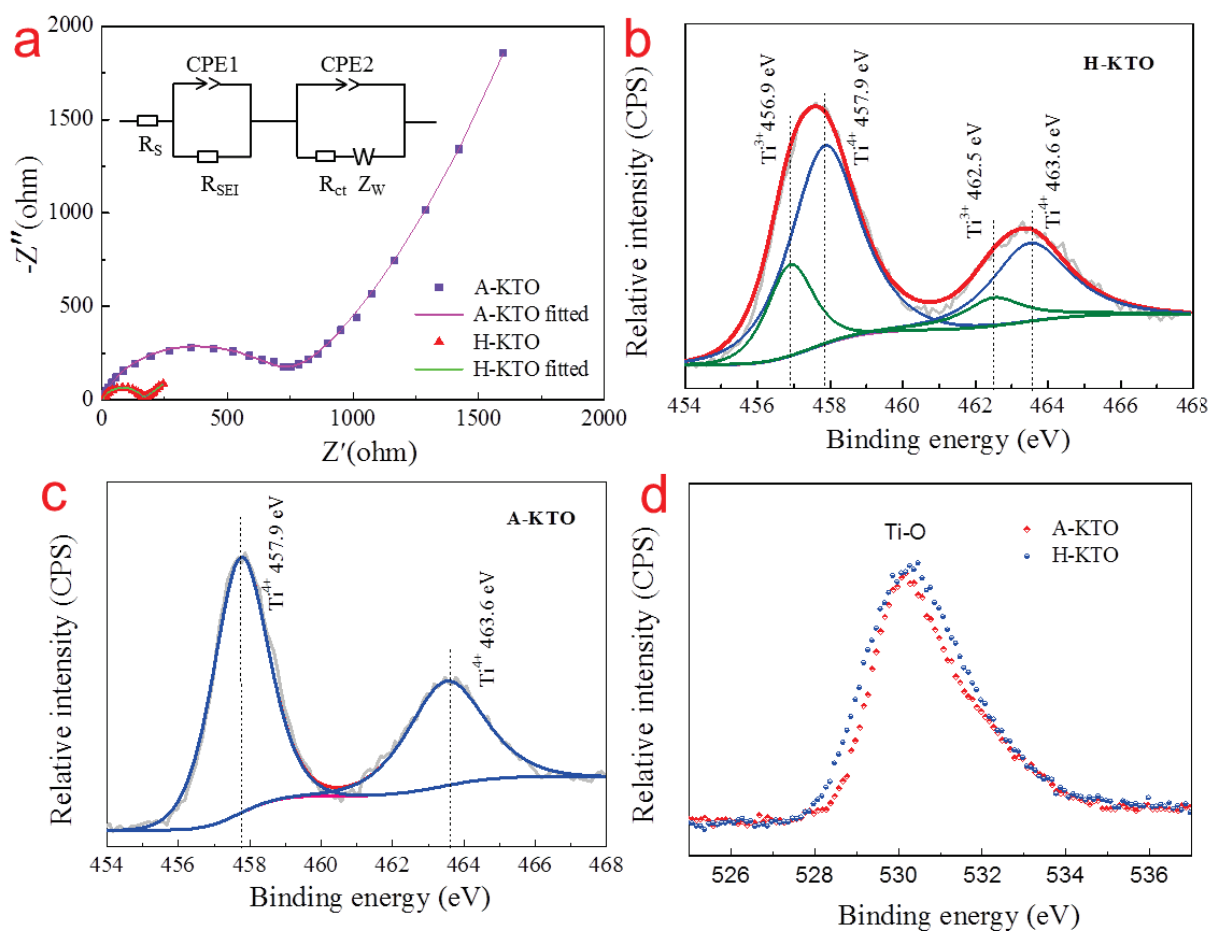determination using the relationship between the peak currents and the sweep rates.

Figure S11. a) Electrochemical impedance spectra of H-KTO and A-KTO at fresh stages, the inset corresponds to the fitting electric circuits. High resolution XPS spectra of Ti 2p, b) H-KTO; c) A-KTO. d) O 1s of H−KTO and A-KTO.
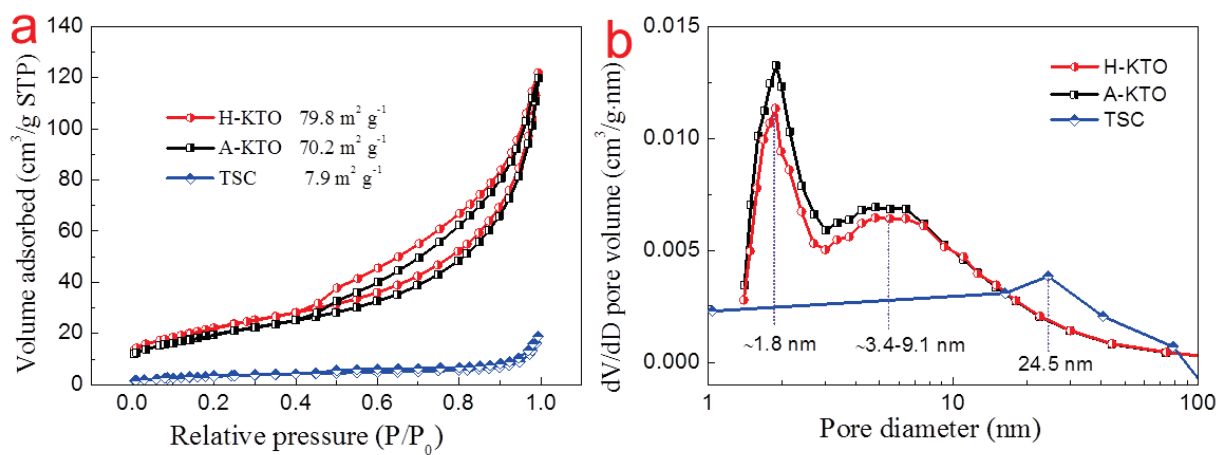
Figure S12. a) Nitrogen adsorption-desorption isotherms and b) the pore size distribution of TSO, A-KTO and H-KTO samples.

(a)

E_i=-1.198 eV E_i=-1.081 eV E_i=0.301 eV

(b)

E_i=-0.358 eV E_i=-0.615 eV E_i=-0.474 eV E_i=-0.500 eV

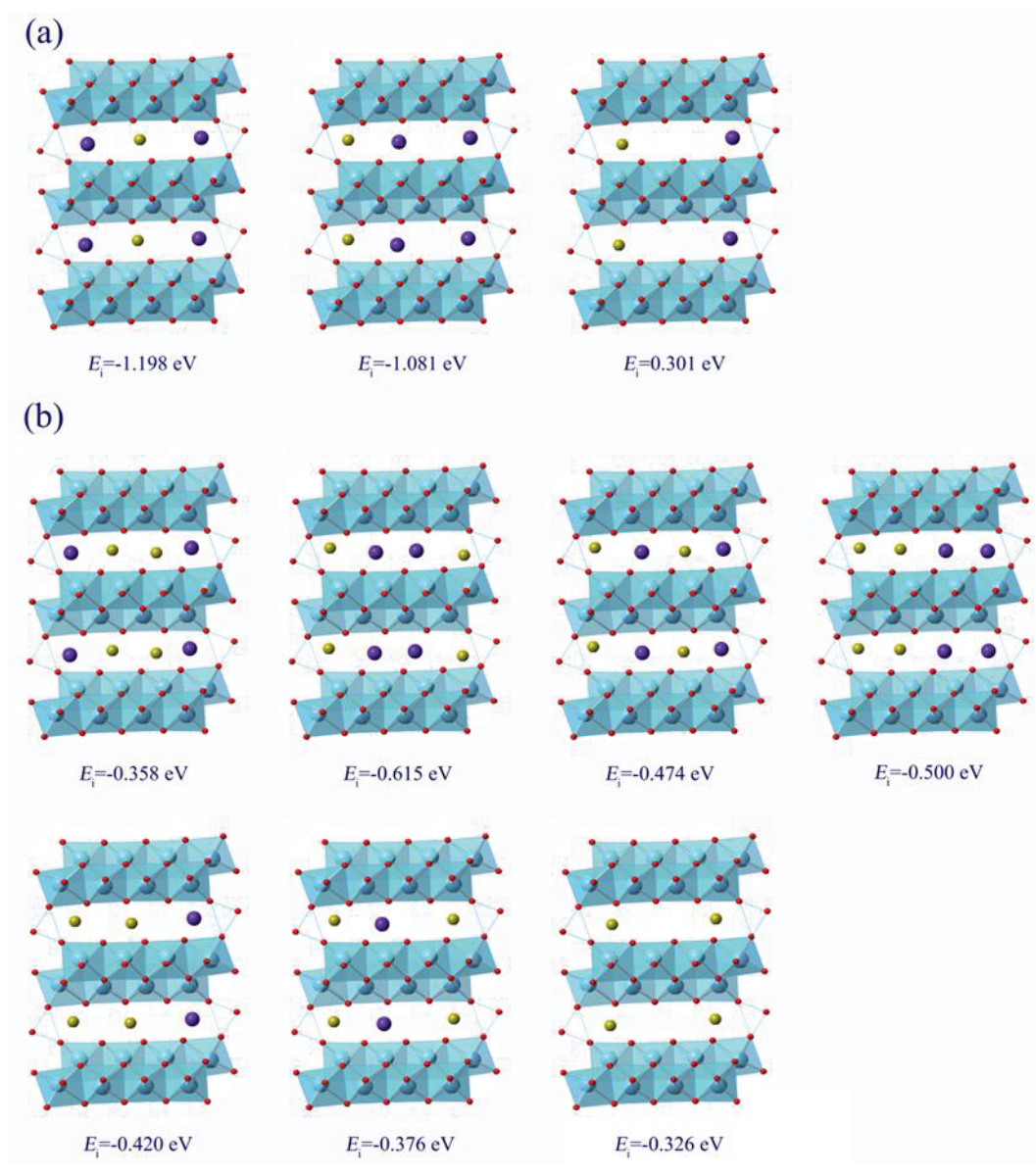E_i=-0.420 eV E_i=-0.376 eV E_i=-0.326 eV

Figure S13. Optimized structures for different numbers of intercalated Na atoms with and without replacing K atoms, a) one Na atom; b) two Na atoms.
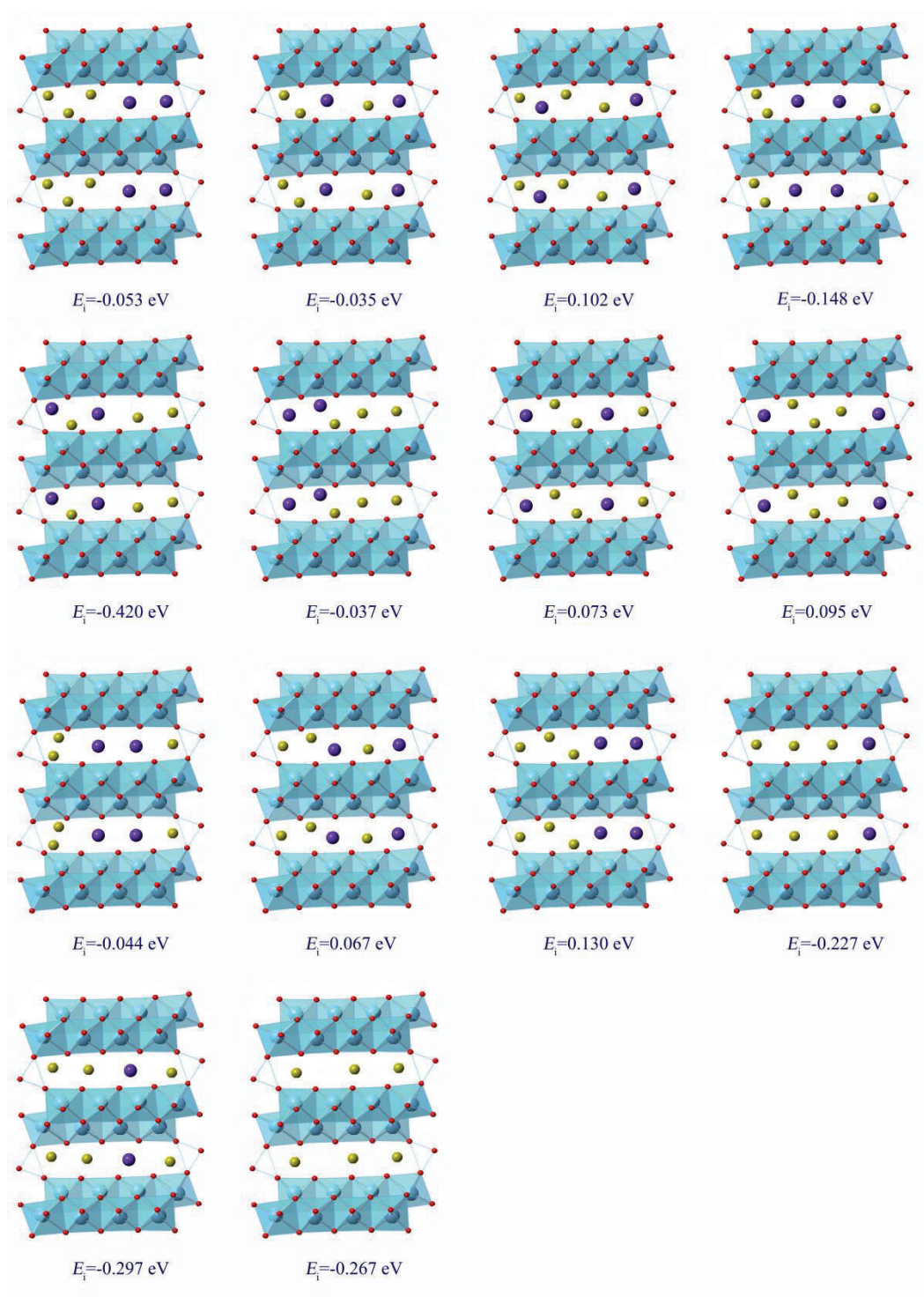
E_i=-0.053 eV E_i=-0.035 eV E_i=0.102 eV E_i=-0.148 eV

E_i=-0.420 eV E_i=-0.037 eV E_i=0.073 eV E_i=0.095 eV

E_i=-0.044 eV E_i=0.067 eV E_i=0.130 eV E_i=-0.227 eV

E_i=-0.297 eV E_i=-0.267 eV

Figure S14. Optimized structures for three intercalated Na atoms with and without replacing K atoms

(a)

$E_i=0.023$ eV	$E_i=-0.026$ eV	$E_i=0.071$ eV	$E_i=-0.033$ eV

$E_i=0.030$ eV	$E_i=0.089$ eV	$E_i=0.127$ eV	$E_i=0.125$ eV

(b)   (c)

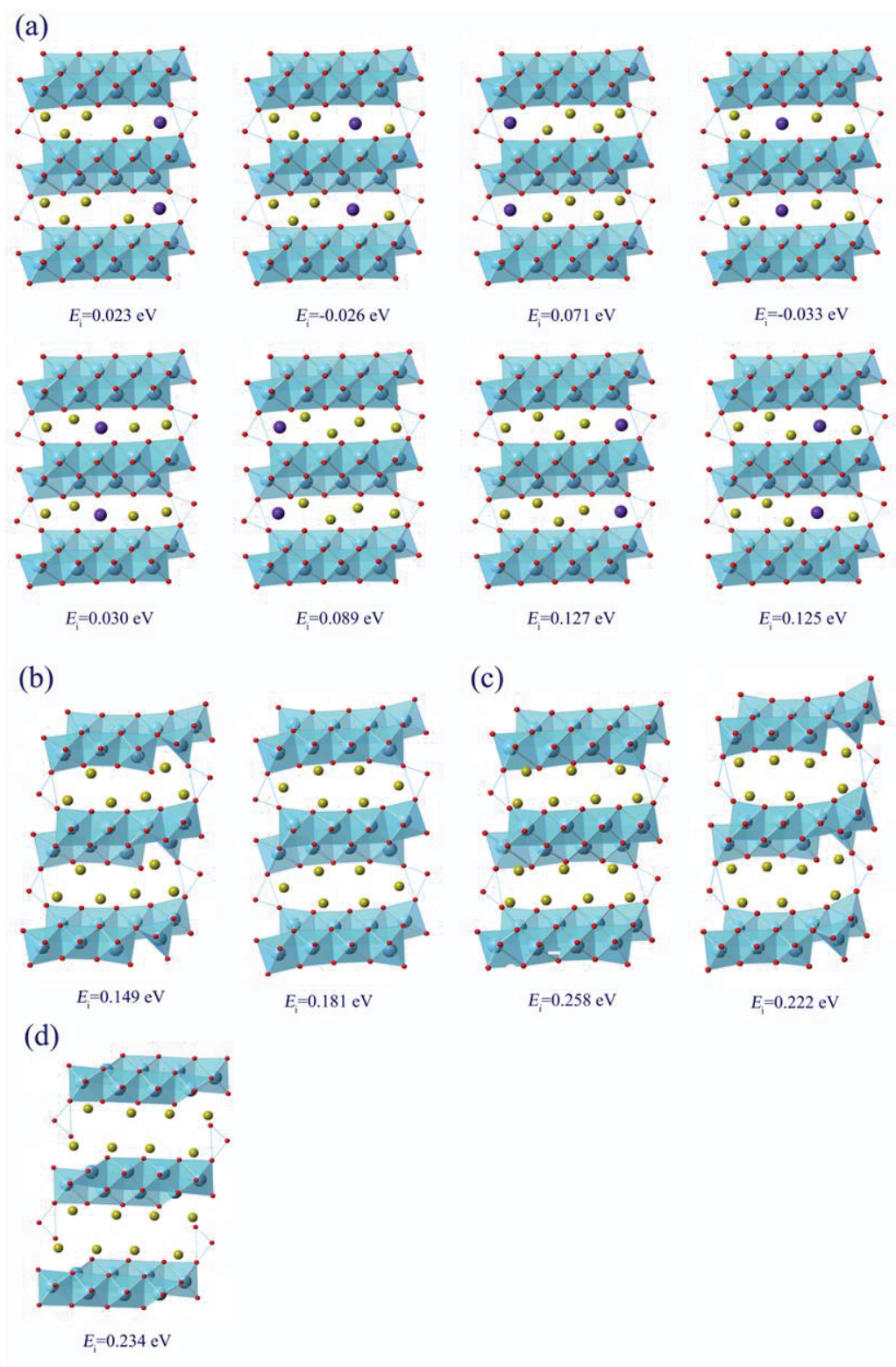|			
$E_i=0.149$ eV	$E_i=0.181$ eV	$E_i=0.258$ eV	$E_i=0.222$ eV

(d)

$E_i=0.234$ eV

Figure S15. Optimized structures for four intercalated Na atoms, a) one K atom; b) six Na atoms; c) seven Na atoms; d) eight Na atoms.
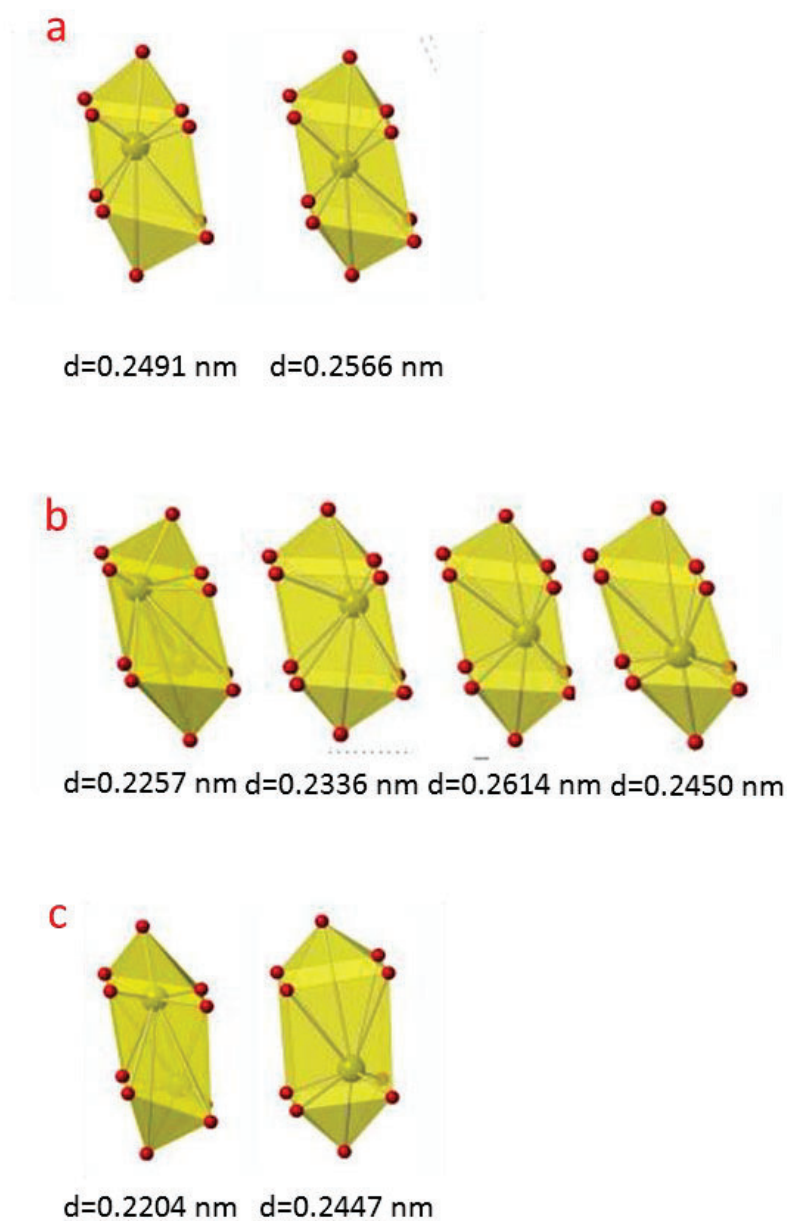
Figure S16. The types of dodecahedron space for Na intercalation, and the under value corresponds to the shortest bond length of Na-O, a) four Na atoms (two types); b) five Na atoms (four types); c) six Na atoms (two types).
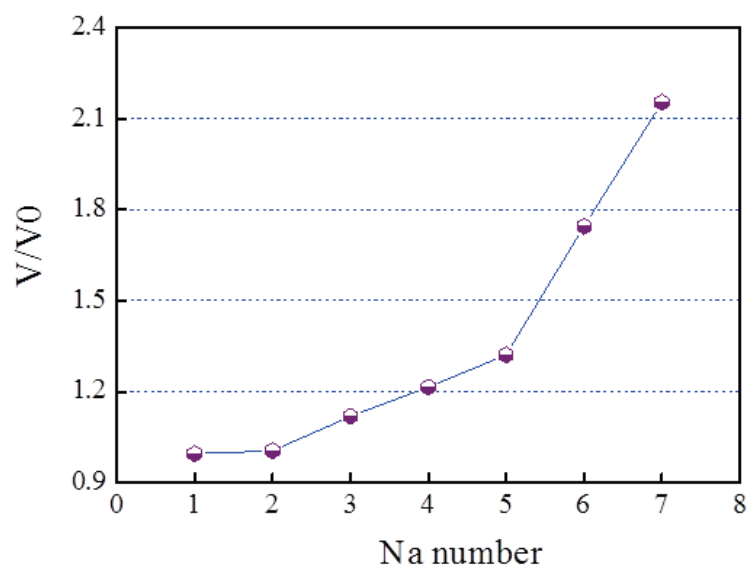
Figure S17. Volume variation dependent on Na intercalation.